

Submitted to The Astrophysical Journal, June 2002

## The Massive Stellar Content in the Starburst NGC 3049: A Test for Hot-Star Models

Rosa M. González Delgado

*Instituto de Astrofísica de Andalucía (CSIC), Apdo. 3004, 18080 Granada, Spain*

*Electronic mail: rosa@iaa.es*

Claus Leitherer

*Space Telescope Science Institute, 3700 San Martin Drive, Baltimore, MD 21218*

*Electronic mail: leitherer@stsci.edu*

Grażyna Stasińska

*LUTH, Observatoire de Paris-Meudon, 92195 Meudon Cedex, France*

*Electronic mail: grazyna.stasinska@obspm.fr*

and

Timothy M. Heckman

*Department of Physics & Astronomy, JHU, Baltimore, MD 21218*

*Adjunct Astronomer at STScI*

*Electronic mail: heckman@pha.jhu.edu*

### ABSTRACT

The objective of this work is twofold: First, we seek evidence for or against the depletion of massive stars in metal-rich starbursts. A second, equally important goal is to perform a consistency test of the latest generation of starburst models in such a high-metallicity environment. We have obtained high-spatial resolution ultraviolet and optical STIS spectroscopy and imaging of the metal-rich nuclear starburst in NGC 3049. The stellar continuum and the absorption line spectrum in the ultraviolet are used to constrain the massive stellar population. The strong,

blueshifted stellar lines of CIV and SiIV detected in the UV spectra indicate a metal-rich, compact, massive ( $\sim 10^6 M_\odot$ ) cluster of age 3 – 4 Myr emitting the UV-optical continuum. We find strong evidence against a depletion of massive stars in this metal-rich cluster. The derived age and the upper mass-limit cut-off of the initial mass function are also consistent with the detection of Wolf-Rayet (WR) features at optical wavelengths. As a second independent constraint on the massive stellar content, the nebular emission-line spectrum is modeled with photoionization codes using stellar spectra from evolutionary synthesis models. The morphology of the nuclear starburst of NGC 3049 from the STIS images indicates a simple geometry for the nebular emission-line region. However, the nebular lines are badly reproduced by 3 – 4 Myr instantaneous bursts, as required by the UV line spectrum, when unblanketed WR and/or Kurucz stellar atmospheres are used. The corresponding number of photons above 24 and 54 eV in the synthetic models is too high in comparison with values suggested by the observed line ratios. Since the ionizing spectrum in this regime is dominated by emission from WR stars, this discrepancy between observations and models is most likely the result of incorrect assumptions about the WR stars. Thus we conclude that the nebular spectrum of high-metallicity starbursts is poorly reproduced by models for WR dominated populations. However, the new model set of Smith et al. (2002) with blanketed WR and O atmospheres and adjusted WR temperatures predicts a softer far-UV radiation field, providing a better match to the data.

*Subject headings:* galaxies: starburst – galaxies: nuclei – galaxies: individual (NGC 3049)–galaxies: stellar content–ultraviolet: galaxies

## 1. Introduction

Starbursts are the site where most of the high-mass star formation occurs. They appear in disks, in bulges and in the nuclei of different types (e.g., spirals, irregulars, or dwarfs) of nearby and distant galaxies. Terlevich (1997) defined starburst galaxies as objects in which the energy output of the starburst dominates that of the host galaxy. Thus, starbursts play a major role in the processes of evolution and formation of galaxies due to their high star-formation activity. They constitute ideal laboratories to investigate some key issues: the formation and evolution of massive stars; the feedback between the interstellar medium and the star formation processes; or the star formation and chemical evolution of the universe.

One important question is which stars form in starbursts. The amount of mass trans-

formed into stars and the mass range of the newly formed stars determine the period of time over which a galaxy can support a starburst phase, and therefore the effect of starbursts on the evolution of galaxies. Thus, it is crucial to know if starbursts have an extreme initial mass function (IMF) with respect to more quiescent systems.

Numerous studies performed in the last few years suggest that the IMF has an universal nature, having a slope close to Salpeter for a mass range between  $5 M_{\odot}$  and  $60 M_{\odot}$  (e.g., references in Gilmore & Howell 1998). However, the IMF in starbursts is still not well known, in particular in high-metallicity environments. Contradictory results have been presented. An extreme IMF for starbursts was suggested by Rieke et al. (1980) in a pioneering work on M82. They proposed a *top heavy* IMF (with a deficit of stars below  $3 - 8 M_{\odot}$ ) to explain the mass-luminosity ratio estimated from K-band photometry and a dynamical mass measurement. This IMF includes a higher fraction of red supergiant stars over red giants and dwarfs than expected for a normal IMF. Their results have been confirmed by Rieke et al. (1993). Satyapal et al. (1997) and Foerster-Schreiber (2000) accounted for the K-band luminosity with a Salpeter IMF and ascribe this apparently discrepant result to the complex morphology of M82 and to dust obscuration in the starburst.

The analysis of the nebular optical+near-infrared (IR) lines indicates the suppression of stars more massive than  $30 M_{\odot}$  (Goldader et al. 1997; Bresolin, Kennicutt, & Garnett 1999; Coziol, Doyon, & Demers 2001). Thornley et al. (2000) used the mid-infrared line ratio of  $[\text{NeIII}]\lambda 15.6/[\text{NeII}]\lambda 12.8$  to measure the hardness of the stellar ionizing radiation. They found that, on average, stars with masses above about  $40 M_{\odot}$  are not present in starburst galaxies, either because they were never formed or because they already have disappeared as a result of aging effects. A complication of the interpretation of  $[\text{NeIII}]/[\text{NeII}]$  are the uncertain stellar evolution models at high metallicity. As pointed out by Thornley et al., observations of gas and stars in the Galactic Center suggest a disagreement between the tracks and the observations, which may be related to the difficulty of defining mass loss, atmospheres, and effective temperatures for metal-rich stars.

On the other hand, the UV-optical continuum from the integrated spectrum of starbursts suggests the formation of such massive stars (Leitherer 1996; Schaerer 2000; González Delgado 2001). This technique has the advantage of probing the stellar light from massive O stars directly, as opposed to a nebular analysis which relies on an indirect measure of the stellar radiation. Using WR-star features, Schaerer et al. (2000) find that a Salpeter IMF extending to masses  $M_{\text{up}} \geq 40 M_{\odot}$  is compatible with the WR-star census observed in metal-rich starbursts. A similar conclusion has been obtained by Bresolin & Kennicutt (2002) and by Pindao et al. (2002) based on the detection of WR features in high-metallicity HII regions.

Most of the results on the IMF have been obtained from a limited number of constraints, through the modeling of a few starburst properties at a specific wavelength. These results can depend strongly on the model ingredients. In particular, the evolutionary synthesis models used to analyze the UV+optical+near-IR properties of the starbursts depend on the stellar tracks, atmospheres, and libraries (see the discussion in Schaerer 2000). In addition, the modeling of the nebular lines depends on the assumptions of the gas geometry, the electron density structure, and the chemical composition of the gas. Thus, inclusion of as many different starburst properties as possible is required for a determination of the IMF.

We have obtained UV and optical spectra and images of the starburst galaxy NGC 3049 with Space Telescope Imaging Spectrograph (STIS) on board of the Hubble Space Telescope (HST) to investigate the possible evidence of depletion of massive stars in metal-rich starbursts. NGC 3049 is a barred spiral galaxy, SB(rs)ab, in the Virgo cluster, known as Mrk 710 in the Markarian & Lipovetskii (1976) catalog. It is also classified as a nuclear starburst (Balzano 1983), a WR galaxy (Conti 1991) and an HII galaxy (Terlevich et al. 1991). Kunth & Schild (1986) first reported the detection of broad emission features at NIII  $\lambda 4640$  and HeII  $\lambda 4686$  produced by WR stars. More recently, Schaerer, Contini, & Kunth (1999) reported the detection of broad CIV  $\lambda 5808$  indicating the presence of WC in addition to late WN stars in the starburst. Due to its nebular emission lines and WR features, NGC 3049 has been observed intensively in the past (e.g. Masegosa, Moles, & del Olmo 1991; Vacca & Conti 1992; Storchi-Bergmann et al. 1994, 1995; Contini 1996; Guseva, Izotov, & Thuan 2000). NGC 3049 is very bright in the far-IR ( $L_{\text{IR}} = 9 \times 10^{42}$  erg s $^{-1}$ ; Heckman et al. 1998) and at UV wavelengths (Kinney et al. 1993). Its IUE spectrum suggests a young stellar population dominating the central ( $20 \times 10$  arcsec) emission (Mas-Hesse & Kunth 1999). Optical images show extended recent star formation along the bar (Mazzarella & Boronson 1993; Contini et al. 1997; Schaerer et al. 1999). Molecular gas has been detected at the center of the galaxy, but no dense gas as traced by the HCN or CS molecules was found (Contini et al. 1997). The oxygen abundance of the nucleus has been estimated by the *strong line* semi-empirical methods because auroral lines (e.g., [OIII]  $\lambda 4363$ , [NII]  $\lambda 5755$ , [SIII]  $\lambda 6312$ ) that are used as electron temperature diagnostics have not been detected in the spectrum. These methods rely, e.g., on  $R_{23} = ([\text{OII}] \lambda 3727 + [\text{OIII}] \lambda 5007) / \text{H}\beta$  or  $[\text{NII}] \lambda 6584 / \text{H}\alpha$  to derive a supersolar oxygen abundance. Vacca & Conti (1992) give  $12 + \log(\text{O}/\text{H}) = 9.08$ , Storchi-Bergmann et al. (1994) give 8.87, Guseva et al. (2000) give 9.03, and Contini (1996) gives 9.05<sup>1</sup>. Even considering the uncertainties associated with these methods, we are confident

---

<sup>1</sup>These abundances have been estimated using the  $R_{23}$  calibration of Edmund & Pagel (1984) or the relation between the oxygen abundance and the  $[\text{NII}] \lambda 6584 / \text{H}\alpha$  ratio derived by van Zee et al (1998), that was obtained also using the Edmund & Pagel calibration

that the metallicity in the nucleus of NGC 3049 is supersolar ( $12 + \log(\text{O}/\text{H}) \geq 8.9$ ).

NGC 3049 has been chosen for this project because previous WFPC (pre-Costar) images at UV wavelengths indicate a relatively simple morphology, with the UV flux dominated by one extremely bright star cluster. This morphology minimizes geometry effect and it makes it easier to study the relation between the stellar and the nebular spectrum, and to search for evidence of an extreme IMF in NGC 3049. In addition, our goal is to perform a critical test of the most sophisticated hot-star models currently available to predict the UV stellar properties and the optical nebular lines in metal-rich starbursts. Our work is organized as follows: the observations and data reduction are in Section 2; in Section 3, we describe the morphology of the UV and optical emission; Sections 4 to 6 deal with the analysis and interpretation of the UV light, UV-optical continuum, and nebular optical lines, respectively. The summary and conclusions are in Section 7.

## 2. Observations and data reduction

We obtained UV and optical spectra and images of NGC 3049 with STIS on board the HST during two visits. In the first visit, on 1998 November 4, NGC 3049 was imaged in the far-UV with the FUV-MAMA detector through the filter F25SRF2 ( $\lambda_c = 1469 \text{ \AA}$ ), and at optical wavelengths with the CCD detector through the filters F28 $\times$ 50LP ( $\lambda_c = 7150 \text{ \AA}$ ) and F28 $\times$ 50OIII ( $\lambda_c = 5007 \text{ \AA}$ ). The total integration time was 900 s in the far-UV. In the optical, the total integration time of 240 s (with the optical longpass filter) and 948 s (with the [OIII] filter) was split in 4 and 2 individual exposures, respectively. The spatial sampling of the FUV-MAMA and CCD detectors is 0.0244 arcsec/pixel and 0.05 arcsec/pixel, respectively. The individual images were calibrated with the standard STScI pipeline, and they were combined with the cosmic-reject command to generate an individual image in the UV and optical (mainly H $\alpha$  plus red continuum), and at [OIII] plus the underlying continuum.

In the second visit, on 1999 January 18, UV and optical spectra of the central region of NGC 3049 were taken. We used the STIS/FUV-MAMA detector with a 52 $\times$ 0.5 arcsec slit and the G140L grating. A total integration time of 11064 s was split in four individual exposures. The spectra cover the wavelength range of 1150 – 1700  $\text{\AA}$  with a dispersion of 0.6  $\text{\AA}$ /pixel, giving a minimum spectral resolution of  $\sim 1 \text{ \AA}$  (for point sources, and larger, up to  $\sim 12 \text{ \AA}$  for extended sources). At optical wavelengths, the STIS/CCD detector was used with a 52 $\times$ 0.1 arcsec slit. Note, however, that the different slit widths used for the optical and UV spectroscopy pose no problem in the analysis of the spectral energy distribution (UV-optical continuum), as we demonstrate in section 5. An exposure with a total integration time of 810 s was taken with the G430L grating covering the wavelength range of 2900 –

5700 Å with a dispersion of 2.7 Å/pixel. This time was split in two individual exposures. In addition, we took a 972 s exposure with the G750M grating centered on 6581 Å and covering 6300 to 6870 Å with a dispersion of 0.6 Å/pixel. This exposure was split in two individual sub-exposures as well. The spectral resolution of the optical spectra is 4 – 5.4 Å and 0.8 – 1.1 Å in the blue and red, respectively. The slit was centered on the brightest nuclear knot and oriented along the bar at P.A. =  $-138^\circ$ . The data extend over more than 8 arcsec with a scale of 0.0244 arcsec/pixel at the UV continuum, and 11 arcsec with a scale of 0.05 arcsec/pixel at the H $\alpha$  line.

The individual spectra were first calibrated with the standard STScI pipeline. Then, the calibrated frames were combined to produce a single two-dimensional spectrum at UV, blue, and red optical wavelengths. We have subtracted a one-dimensional spectrum obtained from the outer part of the UV 2D frame to correct the UV spectrum for the strong geocoronal emission at Ly $\alpha$  and OI  $\lambda$ 1302. This spectrum has only a very weak continuum plus the Ly $\alpha$  and OI and is a good approximation for a sky spectrum. All the spectra have been treated as extended continuum sources when converting from surface brightness units in the 2D frames to flux units ( $\text{erg s}^{-1} \text{ cm}^{-2} \text{ Å}^{-1}$ ). Finally, the spectra have been de-redshifted assuming a heliocentric radial velocity of 1494 km s $^{-1}$ .

In addition, we have retrieved narrowband H $\alpha$  and nearby continuum images from the data archive of the Isaac Newton Group of Telescopes (ING, La Palma). The galaxy was observed on 2001 January 1 with the 1.0 m Jacobus Kapteyn Telescope (JKT) using a 2088 $\times$ 2120 SIT CCD as a detector, with a spatial sampling of 0.33 arcsec/pixel, through an H $\alpha$  ( $\lambda_c = 6594 \text{ Å}$ , FWHM = 44 Å) and a nearby continuum filter ( $\lambda_c = 6656 \text{ Å}$ , FWHM = 44 Å). The integration time was 2400 s in each filter, split in two exposures. The nearby continuum was subtracted iteratively from the H $\alpha$ +continuum image to produce a pure H $\alpha$  image. (Note, however, that this image contains also part of the [NII] emission). The final image is displayed in Figure 1.

### 3. The structure of NGC 3049

#### 3.1. Morphology at the UV and optical wavelengths

The JKT H $\alpha$  image reveals that most of the emission is along the bar and some arcs that emerge from the ends of the bar with a ring-like appearance of 30 arcsec radius (Figure 1). The highest H $\alpha$  surface brightness is at the center of the stellar bar, the nucleus of the galaxy, and at 10 arcsec north-east.

The central 20 $\times$ 20 arcsec far-UV and optical HST images of NGC 3049 are in Figure 2.

Both images show extended emission along the bar, with a similar appearance. However, a clear difference between the two images is the emission at  $\sim 2$  arcsec NE, which is brighter at optical than at UV wavelengths. This could be due to an older stellar population contributing to the red-optical continuum or due to higher obscuration in the NE dimming the UV emission.

The magnitude in the HST system measured in a circular aperture of 0.25 arcsec radius (10 arcsec) is 14.67 and 17.60 (13.40 and 14.45) at UV and optical wavelengths, respectively. Table 1 gives the UV and optical magnitudes of NGC 3049 as a function of the distance obtained from the circular aperture photometry in the UV and optical images.

An expansion of the central  $4 \times 4$  arcsec of NGC 3049 is shown in Figure 3. The [OIII] plus the underlying continuum image is reproduced in this figure as well. The three images suggest that the nuclear starburst is compact, and most of the emission is dominated by a very bright central cluster. However, at least 6 clusters, much weaker, are also detected in the center of the galaxy. The observed properties of these clusters are in Table 2. (The location and precise extraction areas are shown in Figures 3 and 4). The similarity between the UV and optical central morphology indicates that there is not much obscuration at the nucleus of NGC 3049. It looks like hot stars and ionizing gas can be described by a simple geometry. Thus, we expect that the effect of the geometry on the modeling of the nebular lines should be small.

### 3.2. The UV and optical spectra

Figure 4 shows the integrated UV flux as a function of the slit position. The UV flux is dominated by the central cluster, but there are other sources embedded in the extended diffuse emission within the central  $\sim 2.5$  arcsec, as clearly shown in the UV image (Figure 3). As expected from the morphology of the images, the integrated optical continuum (near  $H\alpha$ ) and the  $H\alpha$  emission have a spatial distribution similar to the UV flux.

As a compromise between signal-to-noise and spectral resolution, we have obtained the UV spectra with a slit width of 0.5 arcsec, larger than the 0.1 arcsec width used in the optical spectra. To check the effect of the different slit widths used, we have extracted the spatial profile along P.A. =  $-138^\circ$  in the UV and optical images, simulating a slit of width 0.1 and 0.5 arcsec. Both profiles follow the same spatial distribution, and the spectrum of the central 0.3 arcsec is hardly affected by the slit width mismatch because the central cluster dominating the emission is very compact. The FWHM of the spatial profile corresponding to the central knot is only 0.14 and 0.12 arcsec in the optical and UV images, respectively.

Of course, outside the central cluster, the UV and optical slits are not sampling the same spatial distribution.

Several one-dimensional spectra have been extracted. The windows used at the UV wavelengths are marked in Figure 4. The corresponding one-dimensional red and blue optical spectra (a and b) have been also extracted. Figures 5 and 6 show these spectra. The UV spectrum is dominated by absorption lines formed in the interstellar medium, in the winds, and in the photosphere of massive stars. The main interstellar lines detected in the nuclear spectrum of NGC 3049 are SiII  $\lambda$ 1260, OI+SiII  $\lambda$ 1302, CII  $\lambda$ 1335, SiII  $\lambda$ 1526, FeII  $\lambda$ 1608, and AlII  $\lambda$ 1670; the wind lines are NV  $\lambda$ 1240, SiIV  $\lambda$ 1400, and CIV  $\lambda$ 1550, (but HeII  $\lambda$ 1640 is not clearly detected); and the photospheric lines are OV  $\lambda$ 1371, FeV  $\lambda$ 1360–1380, SiIII  $\lambda$ 1417, CIII  $\lambda$ 1427, and SV  $\lambda$ 1501. The strength of the photospheric lines and the P Cygni profile of the wind lines indicates that a young powerful starburst dominates the UV light. The optical spectra show a strong blue continuum provided by young (O and B) stars, and broad emission lines at  $\sim \lambda$ 4660 Å from WR stars. No absorption lines from an older stellar population have been detected; thus, the optical continuum is only produced by the very young starburst as seen at the UV. The contribution from the bulge population is negligible through this narrow slit. The optical spectra show nebular lines from the Balmer series such as H $\alpha$ , H $\beta$  and H $\gamma$ , low ionization lines such as [OII]  $\lambda$ 3727, [NII]  $\lambda$ 6584,6543, [SII]  $\lambda$ 6717,6731, and the high-excitation line [OIII]  $\lambda$ 5007.

### 3.3. WR-star distribution

As expected, broad emission lines due to WR stars are detected in the STIS blue optical spectrum at  $\sim$ 4660 Å. The STIS red spectrum does not cover the range 5700 – 6300 Å. Therefore we cannot confirm the detection of the red WR bump at 5810 Å, which was previously detected from ground-based observations (Schaerer et al. 1999; Guseva et al. 2000). The blue bump is mainly formed by the blend of NIII  $\lambda$ 4620–4640, CIII  $\lambda$ 4650+CIV  $\lambda$ 4658 and HeII  $\lambda$ 4686 (Figure 6). NV  $\lambda$ 4604 or NIV  $\lambda$ 4507 are not detected, but a weak SiIII  $\lambda$ 4552–4576 blend may be present. This implies that late WN and early and late WC stars are the dominant WR stellar population. However, the weak SiIII blend indicates that some early WN stars can also be present. The detection of CIII  $\lambda$ 4650,  $\lambda$ 5696 (Schaerer et al. 1999) suggests a supersolar metallicity of the starburst because late-type WC stars are only seen in high-metallicity regions (Smith et al. 1991; Phillips & Conti 1992).

No *nebular* HeII  $\lambda$ 4686 is detected in the spectra. However, considering that this line is 0.01 – 0.025 the intensity of H $\beta$  (Guseva et al. 2000), we could not detect it in our STIS spectra even if it were present. We have not unambiguously detected *broad* HeII  $\lambda$ 1640 in



the STIS UV spectra, either. This line must be present, given the presence of the stellar  $\lambda 4686$  line. However, this region is at the edge of the wavelength coverage of the far-UV spectrum, where the S/N is lower and where the continuum placement is challenging.

We have measured the 4660 Å bump in each pixel along the spatial direction to trace the spatial distribution of the WR stars. We find that the flux of the bump peaks at the maximum of the nearby optical continuum. Consequently the WR stars have the same spatial distribution as the main sequence stars. The bump is only detected in 6 pixels ( $\sim 0.3$  arcsec), indicating a very compact spatial distribution of the WR stars.

The total flux of the bump (between 4600 and 4720 Å) is  $1.1 \times 10^{-14}$  erg s $^{-1}$  cm $^{-2}$ , and the equivalent width is  $\sim 14$  Å. This flux is a factor of 2 lower than the flux measured in ground-based observations (Schaerer et al. 1999) with an aperture of 2 arcsec. However, given the sharp spatial distribution of the WR bump and the continuum, we do not think that differences in fluxes can be produced by a more extended WR stellar population. The fluxes of the ground-based spectra have quoted uncertainties of about 30%. Therefore we believe that the discrepancy between the HST and ground-based data is the result of observational uncertainties. We note that the equivalent widths agree rather well, with the HST value being somewhat larger than the ground-based value of 11 Å.

### 3.4. Kinematics of the ionized gas

We constructed the ionized gas velocity curve by fitting a Gaussian to the H $\alpha$  emission line detected along the stellar bar, out to  $-4$  arcsec south-west and  $+11$  arcsec north-east of the nucleus (defined as the peak of the optical continuum). The ionized gas does not follow a rotation curve (Figure 7a), even though our observing angle is close to the position of the line of nodes, P.A. =  $25^\circ$ , and the disk inclination is  $55^\circ$ . Under these conditions we would expect a rotation curve close to the maximum amplitude.

The velocity of the gas close to the nucleus is 1580 km s $^{-1}$ ,  $\sim 90$  km s $^{-1}$  larger than the systemic velocity given in NED, 1494 km s $^{-1}$ , and it is about 40 km s $^{-1}$  lower than the velocity measured by Schaerer et al. (1999). The general large-scale shape is in good agreement with Schaerer et al. (1999). However, our data show more kinematic structure in the central 2 arcsec (Figure 7b). At 0.5 arcsec north-east of the nucleus, the gas is blueshifted by 100 km s $^{-1}$ , and at 1 arcsec, the gas has again the nuclear velocity. Therefore, the gas is both approaching and receding along the line of sight by 100 km s $^{-1}$  within a spatial scale of 1 arcsec.

Two kinematic components are resolved and extended by 0.4 arcsec south-west of the

nucleus, and by 0.1 arcsec at 0.6 arcsec north-east. These two components are also detected in [NII]  $\lambda 6584,6548$  (Figure 8), but not in  $H\beta$  or [OIII]. In the south-west, the second weaker component is blueshifted by  $\sim 60 \text{ km s}^{-1}$  with respect to the main brightest component with a velocity of  $1600 \text{ km s}^{-1}$ . This component may represent a bubble powered by the winds from the massive stars.

Other evidence of the interaction of massive stars with the interstellar medium comes from the UV interstellar lines. Some of these lines are detected at zero redshift (in the observed spectrum *a* and *b*), and thus are associated with gas in the Milky Way. However, other lines, such as SiII  $\lambda 1260$ , OI+SiII  $\lambda 1303$ , CII  $\lambda 1335$ , and SiII  $\lambda 1526$ , form in the interstellar medium of the starburst. We have measured the radial velocity of SiII  $\lambda 1260$  and CII  $\lambda 1335$  with respect to the Milky Way (MW) lines. Their radial velocities indicate blueshifts of about  $210 \text{ km s}^{-1}$  with respect to the redshift given in NED and about  $300 \text{ km s}^{-1}$  with respect to the radial velocity measured in the nebular ionized gas. Thus, the warm interstellar gas in the nuclear starburst of NGC 3049 is outflowing by  $200 - 300 \text{ km s}^{-1}$ . Outflows with similar velocities have been detected in other starburst galaxies (e.g., González Delgado et al. 1998; Kunth et al. 1998; Johnson et al. 2000).

## 4. Modeling the UV light

The absorption lines formed in the wind of massive stars are driven by radiation pressures; their profiles depend on the luminosity of the star (Castor, Abbott, & Klein 1975). Therefore, since there is a well defined stellar mass-luminosity relation, the profiles in the integrated light of a starburst depend on the IMF, star formation history, and age of the stellar clusters (Leitherer, Robert, & Heckman 1995). Thus, the profile shapes of the main wind lines such as NV, SiIV, and CIV can be used to constrain the properties of the starburst.

### 4.1. Description of the models

We compare the observed UV spectra (wind and photospheric lines, and UV continuum flux) to the predictions from evolutionary stellar population models. We use the code STARBURST99 (hereafter SB99; Leitherer et al. 1999) which is optimized to reproduce many properties of active star forming galaxies. The stellar population is parameterized in terms of an IMF which follows a power-law between two mass limits  $M_{\text{up}}$  and  $M_{\text{low}}$ . The stellar population is evolved from the zero-age main sequence using the zero-rotation stellar tracks of the Geneva group (Meynet et al. 1994). The SB99 models use two extreme star

formation histories, an instantaneous burst and constant star formation (csf). The code can use two stellar libraries in this spectral region, depending on the metallicity. One of these libraries is built with IUE spectra of Milky Way stars in the solar vicinity with solar or slightly subsolar metallicity. The O and WR stellar spectra are from the atlas of Robert, Leitherer, & Heckman (1993) and the B spectra from de Mello, Leitherer, & Heckman (2000). The second library has been recently built with an atlas of metal-poor ( $Z \approx 1/4 Z_{\odot}$ ) O stars in the Large and Small Magellanic Clouds (Leitherer et al. 2001). Models are computed for instantaneous bursts between 0 and 10 Myr, and for csf lasting for 10 Myr, and for different assumptions about the slope ( $\alpha = 2.35, 1.5$ ) and upper mass cut-off ( $M_{\text{up}} = 100, 60$ , and  $40 M_{\odot}$ ) of the IMF.

## 4.2. Model results

As the strength of the P Cygni features depends on the mass-loss rate, which is a function of the metallicity (Puls et al. 1996), we have computed models using the solar metallicity stellar tracks and the MW stellar library, and the subsolar stellar tracks ( $Z = 0.008$  and  $0.004$ ) and the Magellanic Clouds stellar library. This has been done to confirm that the starburst has supersolar metallicity instead subsolar. Models with subsolar metallicity and using the MC stellar library predict weaker wind lines than the lines detected in the spectrum of NGC 3049. Thus, the nuclear stellar metallicity of NGC 3049 is at least solar, consistent with the result from the ionized gas. Therefore, the models are computed with the MW stellar library and the stellar evolutionary tracks at  $Z = 0.02$  and  $Z = 0.04$  in order to constrain the star formation history, age, and IMF.

We can use the relative strength of the SiIV P Cygni profile with respect to the P Cygni profiles of CIV and NV in order to constrain the star-formation history of the youngest stellar population. SiIV has a strong profile only in O supergiants, while CIV and NV are strong in O stars of any luminosity class. Thus, SiIV has a strong P Cygni profile if the cluster formed in an instantaneous burst and its age is between 3 and 5 Myr. On the other hand, the profile of CIV depends strongly on the slope and upper mass limit of the IMF.

SiIV is very strong in the nuclear (cluster *b*) spectrum. The intensity of the emission and the depth of the absorption of the profile are only reproduced if many O blue supergiants dominate the UV light, requiring instantaneous burst models. In clusters *c* and *d*, the SiIV is weaker, indicating a lower fraction of O supergiants with respect to O main-sequence stars than in cluster *b*. However, the P Cygni profile is also well fitted by instantaneous burst models. Because cluster *b* dominates the total central UV light, and wind lines are not diluted in extraction *a* with respect to *b*, the best models to predict the wind lines in the

central spectrum are also instantaneous bursts. Therefore, the UV central light is provided by clusters of similar age.

We deduce clusters ages of 3 – 4 Myr from the comparison of the wind profiles with instantaneous burst models if we assume that the stars evolved following the  $Z = 0.02$  or  $Z = 0.04$  stellar tracks. Models with a Salpeter IMF with  $M_{\text{up}} \geq 60 M_{\odot}$  fit well the wind lines; however, models with a flatter Salpeter IMF (and with a larger fraction of massive stars) are also compatible with the observed wind lines (Figure 9). However, because of the strong P Cygni profile of SiIV and CIV, we can rule out clusters younger than 2.5 Myr and older than 4 Myr, and models with very few massive stars (e.g., IMF with  $M_{\text{up}} = 40 M_{\odot}$ ; Figure 10). We conclude, that in spite of the high-metallicity environment in the center of the galaxy, very massive stars formed in these clusters, and they formed with a very small age spread.

We can compare the reddening corrected UV continuum luminosity provided by the clusters with the predictions from evolutionary models for a mass estimate. The UV intrinsic spectral distribution of young unobscured clusters follows a power law ( $F_{\text{UV}} \propto \lambda^{\beta}$ ), with  $\beta$  depends little on the IMF and the star-formation history. A deviation of the exponent from the predicted values can be interpreted as a dust effect. Note, however, that the UV light does not account for low-mass stars. Their contribution must be added by assuming an IMF at the low-mass end. In addition, our estimate depends on the reddening correction applied to the observed UV flux, and therefore on the dust obscuration law.

Using the reddening law of Calzetti et al. (2000), which is an empirical attenuation curve derived for starbursts, we estimate  $E(B - V) = 0.2$  to match the observed spectra with the UV spectral energy distribution (SED) predicted by the models. Because the Galactic foreground extinction is very small,  $E(B - V) = 0.01$ , most of the reddening is intrinsic to the starburst. There is no significant change of the reddening in the center of NGC 3049, as suggested by the same value for the different UV spectra extracted (*a*, *b*, *c*, and *d*).

After correcting for reddening and assuming a distance of 18 Mpc (Vacca & Conti 1992), the UV luminosity at 1500 Å is  $\log L_{1500} = 39.52$  ( $\text{erg s}^{-1} \text{Å}^{-1}$ ) and 39.35 ( $\text{erg s}^{-1} \text{Å}^{-1}$ ) for the spectra *a* and *b*, respectively. Therefore, the mass of the central starburst is  $\sim 10^6 M_{\odot}$ , and the number of O stars in the central cluster is  $\sim 4000$ . This mass is only a factor of two lower than the stellar mass required to account for the total bolometric luminosity (assuming  $\log L_{\text{Bol}} = \log L_{\text{FIR}} = 42.93$  ( $\text{erg s}^{-1}$ )). This cluster, together with the other fainter clusters detected in the UV, can come up for almost half of the IRAS luminosity of NGC 3049, suggesting that a significant fraction of the UV is reprocessed into far-IR luminosity. The stars seen via their spectral lines in the UV are representative of the global starburst. There is

no need to hypothesize an additional, dust obscured population. We can estimate the number of WR stars and the WR/O ratio from the WR blue bump luminosity. The luminosity of the bump after correcting for reddening ( $E(B - V) = 0.2$ ) is  $\log L_{4660} = 38.94$  ( $\text{erg s}^{-1}$ ). This translates into  $\sim 275$  WR stars in the cluster if we assume that the average luminosity of a WN7 star is  $\log L_{4660} = 36.5$  ( $\text{erg s}^{-1}$ ). The resulting WR/O ratio of 0.065 is in agreement with the prediction by an instantaneous burst of age 3 Myr (WR/O = 0.08 for  $Z = 0.02$ ). We also estimated the number total ionizing photons (see Table 2). The corresponding  $\text{H}\beta$  luminosity is in agreement with the observed value (see Section 6.1).

## 5. Modeling the UV-optical continuum

The equivalent width (Ew) of  $\text{H}\beta$  measured in the spectrum *b*, 7 Å, is lower than the Ew reported from ground-based observations, 34 – 36 Å (Vacca & Conti 1992; Schaerer et al. 1999; Guseva et al. 2000), and much lower than the predicted Ew( $\text{H}\beta$ ) for an instantaneous burst between 3 Myr (Ew( $\text{H}\beta$ ) = 200 Å) and 4 Myr (Ew( $\text{H}\beta$ ) = 63 Å) at solar metallicity, for a Salpeter IMF with  $M_{\text{up}} = 100 M_{\odot}$ . This large discrepancy may be caused by an additional stellar population that contributes to the optical continuum flux but not to the ionization. Certainly, the bulge population may contribute significantly to the continuum flux detected in the ground-based observations of Guseva et al. obtained through a slit of 2 arcsec width.

We use the SED of the central cluster of NGC 3049 over the range of  $\sim 1200 - 6800$  Å to find evidence for an additional older stellar population that might dilute the Ew( $\text{H}\beta$ ). However, with the exception of the WR features, we have not detected any other stellar lines at optical wavelengths. The Balmer absorption lines, or the CaII H and K lines, which could indicate a population of B-A stars, are not detected in the spectrum. Thus, this featureless blue optical continuum emitted by the central  $0.1 \times 2$  arcsec could be provided mainly by a single age, young stellar population. Even so, we have compared the shape of the continuum with the models as a further constraint on the stellar population providing the optical continuum flux of the central spectrum.

Although the images and spectra indicate a very compact central cluster (FWHM of the profiles  $\sim 0.12 - 0.14$  arcsec), the optical continuum flux measured through a slit of 0.1 arcsec may represent only some fraction of the total optical continuum flux emitted by the cluster. To estimate this fraction, we have compared the optical continuum flux measured in the spectrum *b* (corresponding to the central  $0.5 \times 0.1$  arcsec;  $2.9 \times 10^{-16} \text{ erg s}^{-1} \text{ Å}^{-1}$  at 6900 Å) with the flux measured in the optical image in an aperture of  $0.5 \times 0.5$  arcsec ( $3.4 \times 10^{-16} \text{ erg s}^{-1} \text{ cm}^{-2} \text{ Å}^{-1}$ ). A direct comparison of these values indicates that the extracted continuum flux fraction through the central  $0.5 \times 0.1$  arcsec spectrum is about

85% of the total flux. The optical continuum flux of the spectrum  $b$  has to be scaled by a factor of  $1.15^2$  for a comparison with the UV continuum. Taking into account this scaling factor, we have merged the UV and optical continua corresponding to the spectrum  $b$ . We have also corrected the continuum flux distribution for reddening with the Calzetti et al. (2000) obscuration law and  $E(B - V) = 0.2$ . We find that the dereddened continuum is very well fitted by the SED of an instantaneous burst of age 3 Myr and formed following a Salpeter IMF with  $M_{\text{up}} = 100 M_{\odot}$ . No additional older stellar population is required to fit the continuum, and the stellar population must contribute very little to the flux detected through a 0.1 arcsec slit. This result contrasts with those obtained based on the analysis of ground-based observations (obtained with a slit width of several arcsec), that claim that a post-starburst stellar population contributes significantly to the optical continuum (Mas-Hesse & Kunth 1999; Schaerer et al. 2000). Probably, this post-starburst stellar population is more spatially extended than the ionizing stars, therefore, it does not contribute significantly to the continuum flux detected in the STIS narrow slit.

The contribution from an additional stellar population to the young burst is not the explanation of the large discrepancy between the STIS observed  $\text{EW}(\text{H}\beta)$  and the value predicted by the 3 – 4 Myr instantaneous burst models. However, the difference can be explained if the ionized gas is more extended than the continuum flux. If the total  $\text{H}\beta$  flux measured from the ground-based observations (scale of  $\sim 100$  pc) is divided by the optical continuum flux near  $\text{H}\beta$  measured in the spectrum  $b$  (scale of a few pc), the  $\text{EW}(\text{H}\beta)$  is  $120 \text{ \AA}$ , which is in perfect agreement with the predicted values for a 3.5 Myr instantaneous burst. There is no need for an extended burst or an older stellar population in the central  $0.5 \times 0.1$  arcsec.

## 6. Modeling the nebular lines

It is well known that starbursts display a spectral dichotomy. As we have described, the UV wavelengths are dominated by wind and photospheric absorption lines from massive stars, and the optical wavelengths by nebular emission lines. Because the stellar winds of non-WR stars are optically thin to the ionizing photons from massive stars, the photons escape and are absorbed by the surrounding interstellar medium. Then, the ionized gas cools down via radiation from the emission lines. Thus, like the stellar UV lines, the emission lines depend on the stellar content of the starburst. However, it is more difficult to constrain the

---

<sup>2</sup>Note that the  $L_{4660}$  estimated in the previous section has to be multiplied by this fraction as well to account for the total flux

age, IMF, and star-formation history of the starburst through the nebular lines because the modeling of the emission lines is a degenerate problem. In addition to the radiation field, the strength of these lines depends on the chemical composition, the density structure, and the geometry of the ionized gas. Even so, photoionization models of various starbursts and HII regions can successfully constrain the stellar content (e.g., García-Vargas et al. 1997 for the HII regions of NGC 7714; González Delgado et al. 1999 for the nuclear starburst of NGC 7714; Luridiana et al. 1999 for NGC 2363; Stasińska & Schaerer 1999 for IZw18; González Delgado & Pérez 2000 for NGC 604; Luridiana & Peimbert 2001 for NGC 5461).

In the present study we perform a critical test of the inputs to the photoionization models, in particular the radiation field of the ionizing stars. The stellar ionizing spectrum is known a priori from the analysis of the UV spectra. Therefore we expect to constrain the IMF and to check if the stellar and the nebular analysis in this high-metallicity starburst lead to similar  $M_{\text{up}}$ . We begin with a description of the observational constraints and the input parameters for the photoionization models.

### 6.1. Observational constraints

The observed quantities to constrain the photoionization models are:

*Geometry of the HII region.* The [OIII] and  $\text{H}\alpha$  images indicate that the region is very compact with a radius of  $\sim 1.2$  arcsec, corresponding to  $\sim 100$  pc. A sphere with a Stromgren radius of  $\sim 100$  pc is a simple geometry that seems adequate to describe the ionized region.

*Hydrogen recombination lines.* The Balmer line intensities depend on the ionizing photon luminosity,  $Q(\text{H})$ . We have estimated  $Q(\text{H})$  from the mass of the cluster, which is derived from the luminosity (see Table 2). This  $Q(\text{H})$  gives an  $\text{H}\beta$  luminosity of  $\log L(\text{H}\beta) \approx 40.1$  ( $\text{erg s}^{-1}$ ). This luminosity agrees well with the measurements of Vacca & Conti (1992) ( $39.9 \text{ erg s}^{-1}$ ) and Schaerer et al. (1999) ( $39.8 \text{ erg s}^{-1}$ ) if we take into account that the narrow long-slit used for the spectroscopic observations, which represents a lower limit to the total  $\text{H}\beta$  flux of the ionized region. On the other hand, Guseva et al. (2000) estimate the total  $\text{H}\beta$  luminosity correcting for slit effects and seeing. They give  $\log L(\text{H}\beta) \approx 40.3$  ( $\text{erg s}^{-1}$ ).

*HeI recombination lines.* The ratio of  $\text{HeI } \lambda 5876/\text{H}\beta$  is very sensitive to the effective temperature of the stars if  $T_{\text{eff}} \leq 40000$  K. Because this ratio depends only on the ratio of the He to H ionizing photons, it must be predicted very accurately. Given the importance of fitting this ratio correctly, we impose that the theoretical and observed ratios must agree within less than 25%. Because our spectral range does not cover the  $\text{HeI } \lambda 5876$  line, we took

the HeI  $\lambda 5876/\text{H}\beta$  ratio from ground-based observations (see Table 3). After inspecting the literature, we consider the ratio of Guseva et al. as the most credible value because they have taken into account the absorption by the stellar population.

*Collisionally excited lines.* Ratios of forbidden over Balmer lines, such as  $[\text{OIII}]\lambda 5007/\text{H}\beta$ ,  $[\text{OII}]\lambda 3727/\text{H}\beta$ ,  $[\text{OI}]\lambda 6300/\text{H}\beta$ ,  $[\text{NII}]\lambda 6584/\text{H}\beta$ , and  $[\text{SII}]\lambda 6717+6731/\text{H}\beta$  depend on the ionization structure on the gas and on the electron temperature. The most useful ratios are those sensitive to the effective temperature of the stars, such as  $[\text{OIII}]\lambda 5007/[\text{OII}]\lambda 3727$ . This ratio must be predicted to within 50%.

*Electron density.*  $N_e$  is determined by the  $[\text{SII}]\lambda 6717/[\text{SII}]\lambda 6731$  ratio. Ground-based observations of this ratio indicate that  $N_e$  is  $\sim 300 \text{ cm}^{-3}$ . From our STIS spectra we measure  $\sim 500 \text{ cm}^{-3}$  in the central 0.3 arcsec.

Table 3 gives all the observed emission line ratios and other additional constraints for the models.

## 6.2. Input parameters and assumptions

We have computed several sets of models using different SEDs as the ionizing radiation field in two different photoionization codes, PHOTO (in the version described in Stasińska & Leitherer 1996) and Cloudy (Ferland 1997, version C96.b2). The reason for using two codes is to perform a consistency check of the results. Even though photoionization codes have been shown before to give similar results at subsolar metallicity (references in Ferland & Savin 2001), the results may diverge at supersolar metallicity due to numerical and physical instabilities under very extreme conditions. However, we find the same general conclusion from both photoionization codes, i.e., the inability to fit the observed emission line ratios with clusters formed 3 – 4 Myr ago containing stars more massive than  $M_{\text{up}} \geq 60 M_{\odot}$  (see below).

The shape of the stellar radiation field (see Section 6.5 for details), the ionizing photon luminosity, the electron density, the inner radius of the sphere, the filling factor, and the chemical composition are the input parameters for the photoionization models to predict the intensity of the emission lines. We always assume that the gas is ionization bounded, and we adopt a fixed ionizing photon luminosity,  $\log Q = 52.45 \text{ (ph s}^{-1}\text{)}$ , as estimated from the UV continuum luminosity of the central starburst. The models reproduce the Balmer recombination lines with this value of  $Q$ . The electron density is constant and equal to  $300 \text{ cm}^{-3}$ .



The central cluster in our STIS images of NGC 3049 is unresolved. We assume a typical cluster size of a few pc, the value derived for young super star clusters in starburst galaxies (Whitmore 2002). The FWHM of the spatial profiles in the UV and optical continuum is  $\sim 9$  pc; therefore the size should be smaller than 9 pc. We adopt 3 pc for the inner radius of the gaseous sphere, but the results would be similar for any value of the inner radius smaller or similar than that.

We assume that the gas is uniformly distributed in small clumps of constant density over the nebular volume and occupies a fraction  $\phi$  of the total volume. A change of  $\phi$  is equivalent to a change of the ionization parameter  $U$ , defined as  $Q/(4\pi R N_e c)$ , where  $Q$  is the ionizing photon luminosity,  $N_e$  the electron density,  $c$  the speed of light and  $R$  the outer radius of the nebula. For a spherical geometry, the average  $U$  is proportional to  $(\phi^2 N_e Q)^{1/3}$ . In our models,  $\phi$  is a free parameter ranging from  $\log \phi = -1.5$  to  $-4.0$  with a step of 0.5. However, this parameter is later fixed at the value that provides a radius of the ionizing front equal to the size of the HII region,  $\sim 100$  pc. Given the relationship between  $\phi(U)$  and the ratio  $[\text{SII}] \lambda 6717 + 6731 / \text{H}\beta$  (González Delgado et al. 1999; González Delgado & Pérez 2000), the value of  $\phi(U)$  has to fit the  $[\text{SII}]/\text{H}\beta$  ratio as well. A filling factor ranging from  $10^{-2}$  to  $10^{-2.5}$  fits the observational constraints, and predicts a radius that is always within  $100 \pm 20\%$  pc.

The radiation field used as input to PHOTO is the SED of the evolutionary synthesis models of Schaerer & Vacca (1998; SV98). They are based on the non-rotating Geneva stellar evolution models with the high mass-loss tracks of Meynet et al. (1994). The SED is built with the CoStar (Schaerer & de Koter 1997) stellar atmosphere models for massive main-sequence stars, which take into account the effects of stellar winds, non-LTE, and line-blanketing. For WR stars, we use the pure He models of Schmutz, Leitherer, & Gruenwald (1992), and the plane-parallel LTE models of Kurucz (1993) for the remaining stars that contribute to the continuum.

Different radiation fields are used as input to Cloudy. They are the SEDs from the SV98 models, and from SB99 (Leitherer et al. 1999). SB99 includes the same stellar evolutionary tracks that SV98, but different stellar atmosphere models. The SB99 code allows users to generate the SED with: i) the stellar atmospheres grid compiled by Lejeune et al. (1997), supplemented with the Schmutz et al. (1992) WR-star models; or ii) the Kurucz (1993) stellar atmosphere models for all stars, including WR stars. SEDs with option i) constitute our standard models, but we ran additional models with option ii) to investigate how our conclusions depend on the stellar atmospheres.

Even though our UV analysis favors the instantaneous burst scenario, the SEDs used here assume two different star-formation histories: instantaneous and continuous star for-

mation at a constant rate. We assume that the slope of the IMF is Salpeter ( $\alpha = 2.35$ ), and the upper mass cut-off is set to 40, 60 and 100  $M_{\odot}$ . We also assume that the stars evolve from the main sequence following the solar ( $Z = 0.02$ ) and twice solar ( $Z = 0.04$ ) metallicity stellar tracks.

The chemical composition of the gas is also a free parameter in the models. There is strong evidence in favor of supersolar metallicity for stars and ionized gas; however, considering the difficulty of making a good abundance estimate in ionized regions where [OIII]  $\lambda 4363$  is not detected, we take the oxygen abundance as a free parameter that changes from half solar to twice solar (0.5, 0.75, 1, 1.5 and 2  $Z_{\odot}$ ) to explore a large range of possible solutions. We scale the other elements following the prescription of McGaugh (1991). However, we generated an extended set models to analyze the effect of dust, in which the abundance of the elements are scaled following the ratios given in Table 14 of the Hazy I Cloudy manual. The effect of dust could be important in high-metallicity HII regions (Shields & Kennicutt 1995). To further check that our conclusions are not dependent on dust effects, we have computed additional Cloudy models with:

- i) Depletion of the gas-phase composition. A fraction of the abundance of the elements may be in a grain phase; thus, the gas phase abundance of the elements is depleted. No absorption or heating by dust are allowed. The depletion factors are those listed in Table 16 of the Hazy I Cloudy manual (Ferland 1997). These factors are based on the depletions listed by Jenkins (1987) and Cowie & Songaila (1986).
- ii) Depletion of the gas-phase composition plus absorption by grains. Models include grains composed of graphite, silicate, and polycyclic aromatic hydrocarbon (PAH). The properties of the grains are listed in Table 17 of the Hazy I Cloudy manual (Ferland 1997). Heating and cooling by dust grains are not allowed.
- iii) Depletion of the gas-phase composition, plus absorption, and heating and cooling by dust grains.

First (Section 6.3), we discuss the results from the standard models (Cloudy+SB99 with stellar atmosphere option i), then (Section 6.4) the effect of dust on the emission-line ratios, and finally (Section 6.5) the models using different stellar atmospheres.

### 6.3. Results from the standard models

Figure 12 shows the HeI  $\lambda 5876/H\beta$ , [OIII]/[OII], [OIII]/ $H\beta$  and [SII]/ $H\beta$  as a function of the age for instantaneous burst models with a Salpeter IMF and  $M_{\text{up}} = 100 M_{\odot}$ . The different symbols correspond to different metallicities of the gas, but we always assume that the stars evolve from the main sequence following the solar tracks ( $Z = 0.02$ ). These models

do not fit the observations if the cluster is 3 – 4 Myr old, and if the IMF is Salpeter-like with  $M_{\text{up}} = 100 M_{\odot}$  because the high-excitation emission-line and HeI/H $\beta$  ratios are higher than observed. The observed ratios suggest that the ionizing radiation field has to be softer than the extreme ultraviolet field predicted by the solar metallicity models.

The emission-line properties of the nebula depend strongly on the electron temperature of the ionized gas. We can modify the thermal balance of the region by changing the gas metallicity. However, changing the metallicity does not help. The HeI/H $\beta$  and [OIII]/H $\beta$  line ratios point out to contradicting solutions. HeI/H $\beta$  requires a low metallicity ( $\leq 0.5 Z_{\odot}$ ), while [OIII]/H $\beta$  and [OIII]/[OII] indicate a high metallicity ( $\geq 2 Z_{\odot}$ ) of the ionized gas. Consequently, ionized gas with a metallicity lower than the solar value is not a possible solution. Alternatively, the observed emission-line ratios can be accounted for by the solar metallicity models if the cluster is  $\sim 2$  Myr old. However, the UV wind lines completely rule out this solution (Figure 10).

Therefore, instantaneous bursts with a Salpeter IMF slope and  $M_{\text{up}} = 100 M_{\odot}$  cannot fit the observed ratios because the radiation field predicted is harder than the radiation seen by the gas. The softness of the SED can be understood if a lower fraction of massive stars is formed in the cluster. Because the photoionization between 3 – 5 Myr is strongly affected by WR stars, the radiation field becomes significantly softer if the number of WR stars decreases considerably with respect to the O stars. The WR/O ratio can be changed by decreasing  $M_{\text{up}}$ . Figure 13 plots the resulting emission-line ratios as a function of the age for  $M_{\text{up}} = 100, 60$  and  $40 M_{\odot}$ .

Only models with  $M_{\text{up}} = 40 M_{\odot}$  ( $60 M_{\odot}$ ) and age  $\sim 2.5$  Myr ( $\sim 2$ – $2.5$  Myr) are close to the observed values. However, a cluster formed with this  $M_{\text{up}}$  ( $M_{\text{up}} = 40 M_{\odot}$ ) will also have a very low fraction of O and blue supergiant stars. Clusters younger than 2.5 – 3 Myr can be ruled out because blue supergiant stars are clearly contributing to the UV continuum. Therefore, the predicted wind lines are very weak in comparison with the observed lines (Figure 10). Moreover, models with a truncated IMF would underpredict the number of WR stars with respect to the observations.

We have also computed models with SEDs for continuous star formation. Again, models with a large fraction of massive stars do not fit the observed emission-line ratios (Figure 14). A solution can be obtained if the extreme ultraviolet is built with a low fraction of WR stars. Models with  $M_{\text{up}} = 40 M_{\odot}$  and constant star formation predict correct HeI/H $\beta$  and collisional emission-line ratios. However, this solution is not consistent with the UV wind lines and the WR numbers.

Similar conclusions are obtained if the SED is built with the  $Z = 0.04$  ( $2 Z_{\odot}$ ) stellar

evolutionary tracks. Again, we cannot find a consistent solution to fit the nebular emission lines and UV wind lines. The extreme UV SED predicted by the evolutionary models containing a large fraction of massive stars, and in particular WR stars, is much harder than the radiation ionizing field seen by the gas. As a result, the photoionization models are not able to predict the low excitation observed in the high-metallicity HII region of NGC 3049.

Although these conclusions are based on the hypothesis that the region is ionization bounded, the result about the inconsistency between UV wind lines and nebular lines does not depend on this hypothesis. Assuming a density bounded HII region does not resolve this inconsistency. It is not certain a priori that there is sufficient nebular matter surrounding the stellar cluster to absorb all the ionizing photons in HII regions. Evidence that some HII regions may be density bounded has been reported previously (e.g., Beckman et al. 2000; Relaño & Peimbert 2002; Castellanos, Díaz & Tenorio-Tagle 2002). However, we note that the  $H\beta$  luminosity obtained under the assumption that all the Lyman photons are absorbed by the nebular gas is compatible with the observed value in NGC 3049. Leaving some room for uncertainties, one can predict the verdict from density bounded models. In order to reproduce the observed size of the HII region, density bounded models should have a slightly different density and filling factor than taken for the ionization bounded models. Whatever assumption is made for the density bounded models (for example, one could construct them to reproduce the observed  $[OIII]/[OII]$  ratio), their  $HeI/H\beta$  ratio will be equal to or larger than predicted by ionization bounded models. Therefore, our conclusions about the inconsistency between UV wind lines and nebular lines are robust in this respect.

#### 6.4. Results from the dusty models

High-metallicity HII regions are regions where a significant amount of dust can exist. Because the electron temperature is low, dust easily produces important changes to the thermal structure of the HII region, and therefore to the emergent optical emission-line spectrum. In this section, we investigate if dusty models are able to fit the observed emission-line ratios in NGC 3049.

Dust can modify the HII thermal structure in several ways: 1) The metals in the gas phase can be depleted onto grains. This depletion tends to increase the electron temperature of the ionized region. 2) Grains can selectively absorb a fraction of the ionizing photons; in this way they modify the radiation field seen by the gas. 3) Grains can provide photoelectric heating of the gas; subsequently the gas can cool down by electron capture. The consequences of dust in metal-rich HII regions have been discussed by Shields & Kennicutt (1995). They found that depletion of the gas-phase abundances introduces the strongest perturbation on

the optical spectrum, and grain heating can be particularly important for enhancing the high-ionization lines.

Because dust can also modify  $Q(\text{He})/Q(\text{H})$ , we have computed models using the SED from SB99 for instantaneous burst models with a Salpeter IMF and  $M_{\text{up}} = 100 M_{\odot}$  and assuming: i) only depletion of the gas-phase abundance and ii) absorption and heating by grains. For an age of 3 – 4 Myr, the predicted HeI  $\lambda 5876/\text{H}\beta$  is  $\leq 10\%$  lower than the ratio predicted by dust-free models, but the collisional emission ratios are higher. Thus, dust cannot reconcile the observed and the predicted emission-line ratios (Figure 15).

### 6.5. Results using SEDs with different stellar atmospheres

Our previous analysis suggests the failure of the SEDs to predict the extreme UV radiation field which is required to reproduce the observed emission lines. SB99 is optimized for young star forming regions and has been successfully used for consistent models at subsolar metallicity. Therefore it seems likely that the predicted SED in the WR phase is too hard in high-metallicity clusters. We have computed additional solar metallicity dust-free instantaneous burst models with i) Kurucz atmospheres in *all* phases and ii) CoStar atmospheres for O and Schmutz atmospheres for WR stars. This allows us to check if the problem is related to the pure-He WR stellar atmosphere models.

At solar metallicity, models using CoStar predicts roughly the same HeI  $\lambda 5876/\text{H}\beta$  as SB99. The high-excitation lines are also similar to SB99 for the Wolf-Rayet phase, but CoStar predicts larger ratios at younger age due to the inclusion of the wind blanketing in the atmospheres of the main-sequence stars. The agreement at 3 – 5 Myr is not surprising because CoStar and SB99 both use the Schmutz unblanketed WR atmosphere. Thus, CoStar models also fail to reproduce the observed emission-line ratios in NGC 3049 (Figure 16). However, SB99 with Kurucz models predict emission line ratios that are similar to the prediction of the standard SB99 models with  $M_{\text{up}} = 40 M_{\odot}$  (Figure 16). Although these models fit the collisional lines, they underpredict the HeI  $\lambda 5876/\text{H}\beta$  if the cluster is 3 – 4 Myr old. This suggests that the static Kurucz atmospheres are equally inadequate for modeling the WR fluxes. This is well known since the pioneering work of Hillier (1987).

We conclude that pure-He atmosphere models are not adequate for predicting HeI  $\lambda 5876/\text{H}\beta$  and the high-excitation emission-line ratios in high-metallicity HII regions. The new generation of WR atmospheres with line-blanketing calculated by Smith, Norris, & Crowther (2002) can potentially solve this problem. These atmospheres include the most important metals and have a different density and temperature structure in comparison with

the Schmutz models. When coupled with Starburst99, the models of Smith et al. give a softer far-UV radiation field at high metallicity. This is the result of the combination of three effects: i) inclusion of blanketing suppresses the far-UV flux; ii) a higher wind density leads to recombination shortward of 228 Å; iii) the WR core temperature of the evolutionary tracks was found to be too high to be compatible with the new atmospheres. Smith et al find that effect i) is more important for late WR stars, whereas effect ii) dominates for early WR stars. The third effect is the result of different temperature definitions in the evolution and atmosphere models. It can only be calibrated empirically, e.g., by comparing the emergent radiation field to observations. Smith et al. performed an initial calibration and provide a recipe for the adjustment of the evolutionary temperatures. The new models must produce less ionizing radiation at frequencies above the HeII ionizing limit than the Schmutz atmospheres in order not to overpredict the high-excitation ratios. On the other hand, their  $Q(\text{He})/Q(\text{H})$  must be high enough in order not to underestimate HeI  $\lambda 5876/\text{H}\beta$  as the Kurucz atmospheres do. A new version of SB99 including the new set of the stellar atmospheres prepared by Smith et al. was released on 2002 July 23. SEDs obtained with these blanketed WR and O stellar atmospheres at solar and two solar metallicities have been applied to NGC 3049. The results are shown in Figure 17. As it was expected, the models predict lower HeI  $\lambda 5876/\text{H}\beta$  and lower high-excitation collisional lines than the Schmutz et al. unblanketed WR atmospheres and are closer to the observed values. This comparison of the models with NGC 3049 largely supports the view that the softening of the far-UV radiation field at high metallicity is not only a consequence of the inclusion the line-blanketing effect but also of the coupling between the WR temperature of the evolutionary tracks and the new atmospheres. Future tests on high metallicity HII regions will have to confirm and refine the calibration between these two different temperatures proposed by Smith et al.

## 7. Summary and Conclusions

We have obtained HST ultraviolet and optical STIS spectroscopic and imaging observations of the metal-rich starburst NGC 3049. These data are interpreted using evolutionary synthesis models optimized for star forming regions, which allow us to constrain the stellar content of the nuclear starburst. From the analysis of the UV-optical continuum and the optical emission lines we have obtained the following results:

- The nuclear starburst in NGC 3049 is very compact. The UV-optical continuum is dominated by a central cluster that is unresolved in the UV and optical STIS images. The FWHM of the spatial profiles is only  $\sim 0.1$  arcsec, corresponding to 9 pc for a distance of 18 Mpc.

- The central UV flux shows strong wind (CIV, SiIV, NV) and photospheric lines (OV  $\lambda 1371$ , FeV  $\lambda 1360$ -1380, SiIII  $\lambda 1417$ , CIII  $\lambda 1427$ , and SV  $\lambda 1501$ ). These lines suggest a powerful starburst. The modeling of the continuum and stellar absorption lines indicates that a high-metallicity ( $Z = 0.02 - 0.04$ ) 3 – 4 Myr old instantaneous burst with a Salpeter IMF and  $M_{\text{up}} = 100 M_{\odot}$  fits the central 0.5 arcsec spectrum observed in the UV. The mass estimated for the cluster is  $\sim 10^6 M_{\odot}$ , if the extinction toward the cluster is  $E(B - V) = 0.2$ . The reddening-corrected luminosity of this cluster accounts for almost half of the far-IR luminosity of NGC 3049. The massive stars in this cluster provide enough photons ( $\log Q = 52.30$  (ph s $^{-1}$ )) to explain the observed nuclear H $\alpha$  luminosity. Models with very few massive stars (e.g., with  $M_{\text{up}} \leq 40 M_{\odot}$ ) are not able to fit the UV stellar lines. The analysis of the central 1.2 arcsec UV flux also indicates that there is no significant change of the extinction and a very small age spread.
- The central 0.3 arcsec in the optical shows WR features at 4660 Å. These observations confirm previous results (Schaerer et al 1999; Guseva et al 2000) that late WN and early and late WC stars are the dominant WR stellar population. The total luminosity of the bump is  $9 \times 10^{38}$  erg s $^{-1}$  if the stellar reddening is  $E(B - V) = 0.2$ , and the Ew of the bump is 14 Å. This luminosity is provided by  $\sim 275$  WR stars. A WR/O ratio equal to 0.065 is estimated for the cluster. This ratio and the Ew of the bump is in very good agreement with the predictions of the evolutionary models for a 3 – 4 Myr old high-metallicity starburst. Therefore the number of WR stars is correctly predicted by the stellar evolution models.
- We have not detected any absorption lines that could indicate the presence of red supergiants, or an intermediate or old stellar population. The blue optical continuum of the central  $0.5 \times 0.1$  arcsec is well fitted by a 3 Myr old instantaneous burst with  $E(B - V) = 0.2$ , as predicted by the UV continuum. Thus, no additional older stellar population contributes significantly to the nuclear optical continuum.
- The Ew of the H $\beta$  lines is only 7 Å. This is lower than the values of 200 – 60 Å predicted by a 3 – 4 Myr instantaneous burst model. However, this discrepancy is naturally explained if the ionized gas is more extended than the compact cluster.
- Two kinematic components are resolved in the H $\alpha$  emission line. These two components are extended by  $\sim 30$  pc south-west of the maximum of the continuum, and by  $\sim 8$  pc at  $\sim 50$  pc north-east. The second component is blueshifted  $\sim 60$  km s $^{-1}$  with respect to brightest main component. It may represent a bubble powered by the winds from massive stars. Additional evidence for an outflow of the interstellar medium comes from the blueshift of 200 km s $^{-1}$  of the UV interstellar lines with respect to the radial

velocity reported by NED of  $300 \text{ km s}^{-1}$  with respect to the nebular optical radial velocity.

- The modeling of the nebular emission lines failed to constrain the hot stellar content of the nuclear starburst of NGC 3049. The models which predict emission-line ratios in agreement with the observations contain very few massive stars. This result, which is clearly in contradiction with the UV spectrum, would be in line with previous suggestions for a depletion of massive stars in the IMF of metal-rich starbursts. However, this conclusion is an artifact of the failure of the population synthesis models to predict the ionizing radiation field. Most likely, the overly hard radiation field results from the failure of the currently available WR atmosphere grid. The new model set of Smith et al. (2002) includes blanketing and uses different temperature and density structures. These models applied to NGC 3049 predict a softer far-UV radiation field and provide a better match to the data.

The CoStar and SB99 models predict  $\text{HeI } \lambda 5876/\text{H}\beta$  and  $[\text{OIII}]/[\text{OII}]$  ratios that are higher than observed if the ionizing radiation is provided by a 3 – 4 Myr old cluster formed with a Salpeter IMF and  $M_{\text{up}} = 100 M_{\odot}$ . SEDs using only the Kurucz atmospheres can adequately predict the collisional line ratios but they underpredict  $Q(\text{He})/Q(\text{H})$ . Thus extended atmospheres are required but the currently available pure He WR models are inadequate to reproduce the nebular spectrum of high-metallicity starbursts in the WR phase.

## Acknowledgments

We thank Gary Ferland for kindly making his code available, Enrique Pérez and Miguel Cerviño for their comments from a thorough reading of the paper, Daniel Schaerer, the referee, for his detailed and useful report, and Linda Smith for sending us their paper in advance of publication, and making their new version of SB99 available. This work was supported by Spanish projects AYA-2001-3939-C03-01 and by HST grants GO-7513.01-96A from the Space Telescope Science Institute, which is operated by the Association of Universities for Research in Astronomy, Inc., under NASA contract NAS5-26555.



## REFERENCES

- Balzano, V.A. 1983, *ApJ*, 268, 602
- Beckman, J.E., Rozas, M., Zurita, A., Watson, R.A., & Knapen, J.H. 2000, *AJ*, 119, 2728
- Bresolin, F., & Kennicutt, R.C. 2002, *ApJ*, 572, 838
- Bresolin, F., Kennicutt, R.C., & Garnett, D.R. 1999, *ApJ*, 510, 104
- Calzetti, D., Armus, L., Bohlin, R.C., Kinney, A.L., Koornneef, J., & Storchi-Bergmann, T. 2000, *ApJ*, 533, 682
- Castor, J.I., Abbott, D.C. & Klein, R.I. 1975, *ApJ*, 195, 157
- Castellanos, M., Díaz, A.I. & Tenorio-Tagle, G. 2002, *ApJ*, 565, 79
- Conti, P. 1991, *ApJ*, 377, 115
- Contini, T. 1996, Ph. D. Thesis, Université Paul Sabatier, Toulouse, France
- Contini, T., Wozniak, H., Considère, S., & Davoust, E. 1997, *A&A*, 324, 41
- Cowie, L.L., & Songaila, A., 1986, *ARAA*, 24, 499
- Coziol, R., Doyon, R., & Demers, S. 2001, *MNRAS*, 325, 1081
- de Mello, D.F., Leitherer, C., & Heckman, T.M. 2000, *ApJ*, 530, 251
- Edmund, M.G., & Pagel, B.E.J. 1984, *MNRAS*, 211, 507
- Ferland G.J. 1997, *Hazy, a Brief Introduction to Cloudy*, University of Kentucky, Department of Physics and Astronomy Internal Report
- Ferland G.J. & Savin, D.W. 2001, in *Spectroscopic Challenges of Photoionized Plasmas*, ed. G.J. Ferland & D.W. Savin (San Francisco: ASP), 113
- Foerster-Schreiber, N.M., 2000, *New Astronomy Review*, 44, 263
- García-Vargas M.L., González-Delgado R.M., Pérez E., Alloin D., Díaz A.I., & Terlevich E. 1997, *ApJ*, 478, 112
- Gilmore, G., & Howell, D. 1998, *The Stellar Initial Mass Function*, ed. G. Gilmore & D. Howell (San Francisco: ASP), 61
- Goldader, J.D., Joseph, R.D., Doyon, R., & Sanders, D.B. 1997, *ApJ*, 474, 104

- González Delgado, R.M. 2001, in *Extragalactic Star Clusters*, ed. E.K. Grebel, D. Geisler, & D. Minniti (San Francisco: ASP), in press (astro-ph/0106297)
- González Delgado, R.M., García-Vargas M.L., Goldader J., Leitherer C., & Pasquali A. 1999, *ApJ*, 513, 707
- González Delgado, R.M., Leitherer, C., Heckman, T., Lowenthal, J. D., Ferguson, H. C., Robert, C. 1998, *ApJ*, 505, 174
- González Delgado, R.M., & Pérez, E. 2000, *MNRAS*, 317, 64
- Guseva, N., Izotov, Yu.I., & Thuan, T.X. 2000, *ApJ*, 531, 776
- Heckman, T.M., Robert, C., Leitherer, C., Garnett, D.R., & van der Rydt, F. 1998, *ApJ*, 503, 646
- Hillier, D. J. 1987, *ApJS*, 63, 947
- Jenkins, E.B. 1987, in *Interstellar Processes*, ed. D. Hollenbach & H. Thronson (Dordrecht: Reidel), 533
- Johnson, K.E., Leitherer, C., Vacca, W.D., & Conti, P.S. 2000, *AJ*, 120, 1273
- Kinney, A.L., Bohlin, R.C., Calzetti, D., Panagia, N., & Wyse, R.F.G. 1993, *ApJS*, 86, 5
- Kunth, D., Mas-Hesse, J. M., Terlevich, E., Terlevich, R., Lequeux, J., Fall, M. 1998, *A&A*, 334, 11
- Kunth, D., & Schild, H. 1986, *A&A*, 169, 71
- Kurucz, R. L. 1993, CD-ROM 13, *ATLAS9 Stellar Atmosphere Programs and 2 km/s Grid* (Cambridge: Smithsonian Astrophys. Obs.)
- Leitherer, C. 1998, in *The Stellar Initial Mass Function*, ed. G. Gilmore & D. Howell (San Francisco: ASP), 61
- Leitherer C., Leão, J.R.S., Heckman, T.M., Lennon, D.J., Pettini, M., & Robert C. 2001, *ApJ*, 550, 724
- Leitherer C., Schaerer D., Goldader J.D., González Delgado R.M., Robert C., Foo Kune D., de Mello D.F., Devost D., & Heckman T.M. 1999, *ApJS*, 123, 3
- Leitherer C., Robert, C., & Heckman, T.M. 1995, *ApJS*, 99, 173

- Leitherer C., Vacca W.D., Conti P.S., Filippenko A.V., Robert C., & Sargent W.L.W. 1996, *ApJ*, 465, 717
- Lejeune T., Buser R., & Cuisinier F. 1997, *A&AS*, 125, 229
- Lejeune, T., Cuisinier, F., & Buser, R. 1996, in *From Stars to Galaxies: The Impact of Stellar Physics on Galaxy Evolution*, ed. C. Leitherer, U. Fritze-von Alvensleben, & J. Huchra (San Francisco: ASP), 94
- Luridiana V., & Peimbert M. 2001, *ApJ*, 553, 633
- Luridiana V., Peimbert M., & Leitherer C. 1999, *ApJ*, 527, 110
- Markarian, B.E., & Lipovetskii, V.A. 1976, *Astrofizika*, 12, 389
- Mas-Hesse, J.M., & Kunth, D. 1999, *A&A*, 349, 765
- Masegosa, J., Moles, M., & del Olmo, A. 1991, *A&A*, 244, 273
- Mazzarella, J.M., & Boronson, T.A. 1993, *ApJS*, 85, 27
- McGaugh, S.S. 1991, *ApJ*, 380, 140
- Meynet, G., Maeder, A., Schaller, G., Schaerer, D., & Charbonnel, C. 1994, *A&AS*, 103, 97
- Pindao, M., Schaerer, D., González Delgado, R.M., & Stasinska, G., 2002, *A&A*, submitted
- Phillips, A.C., & Conti, P.S. 1992, *ApJ*, 395, L91
- Puls, J., Kudritzki, R.-P., Herrero, A., Pauldrach, A.W.A., Haser, S.M., Lennon, D.J., Gabler, R., Voels, S.A., Vílchez, J.M., Wachter, S., & Feldmeier, A. 1996, *A&A*, 305, 171
- Relaño, M., Peimbert, M., & Beckman, J. 2002, *ApJ*, 564, 704
- Rieke, G.H., Lebofsky, M.J., Thompson, R.I., Low, F.J., & Tokunaga, A.T. 1980, *ApJ*, 238, 24
- Rieke, G.H., Loken, K., Rieke, M.J., & Tamblyn, P. 1993, *ApJ*, 412, 99
- Robert C., Leitherer C., & Heckman T.M. 1993, *ApJ*, 418, 749
- Satyapal, S., Watson, D.M., Pipher, J.L., Forrest, W.J., Greenhouse, M.A., Smith, H.A., Fischer, J., & Woodward, C.E. 1997, *ApJ*, 483, 148

- Schaerer, D. 2000, in *Stars, Gas and Dust in Galaxies: Exploring the Links*, ed. D. Alloin, K. Olsen, & G. Galaz (San Francisco: ASP), 99
- Schaerer, D., Contini, T., & Kunth, D. 1999, *A&A*, 341, 399
- Schaerer, D., & de Koter, A. 1997, *A&A*, 322, 598
- Schaerer, D., Guseva, N.G., Izotov, Yu.I., & Thuan, T.X. 2000, *A&A*, 362, 53
- Schaerer, D., & Vacca, W.D. 1998, *ApJ*, 497, 618
- Schmutz W., Leitherer C., & Gruenwald R.B. 1992, *PASP*, 104, 1164
- Shields, J.C., & Kennicutt, R.C. 1995, *ApJ*, 454, 807
- Smith, L.F., Shara, M.M., & Moffat, A.F.J. 1996, *MNRAS*, 281, 163
- Smith, L.J., Norris, R.P.F., & Crowther, P.A. 2002, *MNRAS*, accepted
- Stasińska G., & Leitherer C. 1996, *ApJS*, 107, 661
- Stasińska G., & Schaerer D. 1999, *A&A*, 351, 72
- Stasińska G., Schaerer, D., & Leitherer C. 2001, *A&A*, 370, 1
- Storchi-Bergman, T., Calzetti, D., & Kinney, A.L. 1994, *ApJ*, 429, 572
- Storchi-Bergman, T., Kinney, A.L., & Challis, P. 1995, *ApJS*, 98, 103
- Terlevich, R. 1997, *Rev. Mex. A&A Conf. Series*, 6, 1
- Terlevich, R., Melnick, J., Masegosa, J., Moles, M., & Copetti, M.V.F. 1991, *A&AS*, 91, 285
- Thornley, M.D., Forster Schreiber, N.M., Lutz, D., Genzel, R., Spoon, H. W. W., Kunze, D., & Sternberg, A. 2000, *ApJ*, 539, 641
- Vacca, W.D., & Conti, P. 1992, *ApJ*, 401, 543
- van Zee, L., Salzer, J.J., Haynes, M.P., O'Donoghue, A.A., & Balonek, T.J. 1998, *AJ*, 116, 2805
- Whitmore, B.C. 2002, in *A Decade of HST Observations*, ed. M. Livio, K. S. Noll, & M. Stiavelli (Cambridge: CUP), in press

Table 1. UV (F25RSF2) and Optical (F28×50LP) aperture photometry of NGC 3049

Radius (arcsec)	UV Flux ( $10^{-15}$ erg s $^{-1}$ cm $^{-2}$ Å $^{-1}$ )	UV mag	Radius (arcsec)	Opt. Flux ( $10^{-15}$ erg s $^{-1}$ cm $^{-2}$ Å $^{-1}$ )	Opt. mag
0.123	3.62	15.00	0.10	0.18	18.23
0.247	4.92	14.67	0.25	0.33	17.60
0.494	6.71	14.33	0.50	0.50	17.15
0.741	8.41	14.09			
0.988	9.39	13.97	1.0	0.80	16.64
1.235	10.11	13.89			
1.482	10.54	13.84	1.5	1.06	16.34
1.729	10.89	13.81			
1.976	11.25	13.77	2.0	1.35	16.07
2.223	11.55	13.74			
2.470	11.94	13.71	2.5	1.76	15.79
3.705	13.17	13.60	3.5	2.43	15.44
			4.0	2.72	15.31
			4.5	3.01	15.20
4.940	13.91	13.54	5.0	3.38	15.11
6.175	14.46	13.50			
7.410	14.91	13.47	7.5	4.39	14.79
8.645	15.38	13.43			
9.880	15.89	13.40	10.0	5.24	14.60

Table 2. UV properties of the different extracted one-dimensional UV spectra that are marked in plot 3 and 4.

Spectrum	Extraction ( $\pm$ arcsec)	Flux $_{1500}$ ( $10^{-15}$ erg s $^{-1}$ cm $^{-2}$ Å $^{-1}$ )	$\log L_{1500}$ (erg s $^{-1}$ Å $^{-1}$ )	Mass ( $10^6$ M $_{\odot}$ )	$\log Q$ (ph s $^{-1}$ )
<i>a</i>	1.275	12	39.52	1.5	52.45
<i>b</i>	0.25	8.2	39.35	1	52.30
<i>c</i>	0.125	1.1	38.49		
<i>d</i>	0.125	1.0	38.42		
<i>e</i>	0.125	0.2	37.74		

Table 3. Observed emission-line ratios

line	Guseva et al.	Schaerer et al.	Vacca & Conti	STIS ( <i>a</i> )	STIS ( <i>b</i> )
[OII] $\lambda$ 3727/H $\beta$	1.26	—	1.72	1.1	1.2
[OIII] $\lambda$ 5007/H $\beta$	0.322	0.338	0.321	0.36	0.45
HeI $\lambda$ 5876/H $\beta$	0.104	0.133	0.091	—	—
[OI] $\lambda$ 6300/H $\beta$	—	0.023	—	—	—
[NII] $\lambda$ 6584/H $\beta$	1.074	—	1.08	1.23	1.31
[SII] $\lambda$ 6717/H $\beta$	0.319	—	0.308	0.21	0.19
[SII] $\lambda$ 6731/H $\beta$	0.279	—	0.259	0.23	0.22
Ew(H $\beta$ ) (Å)	35.9	34	35.1	12.4	7
log $L$ (H $\beta$ ) (erg s $^{-1}$ )	40.3	39.80	39.90	—	—

Fig. 1.— Ground-based  $H\alpha$  image observed with the JKT. The  $H\alpha$  emission is detected along the stellar bar and in a ring of 30 arcsec radius. North is up and east to the left. This is the orientation in all the images.

Fig. 2.— HST+STIS images of NGC 3049: a) UV wavelength with the FUV-MAMA detector and the filter F25SRF2 ( $\lambda_c = 1469 \text{ \AA}$ ). The sampling is 0.025 arcsec/pixel. b) Optical wavelength with the CCD detector and the filter F28 $\times$ 50LQ ( $\lambda_c = 7150 \text{ \AA}$ ). The sampling is 0.05 arcsec/pixel.

Fig. 3.— Central 4 $\times$ 4 arcsec emission of NGC 3049 at: a) UV wavelengths. b) Optical wavelengths. c) [OIII] emission line plus the underlying continuum. The nuclear emission is dominated by a central cluster.

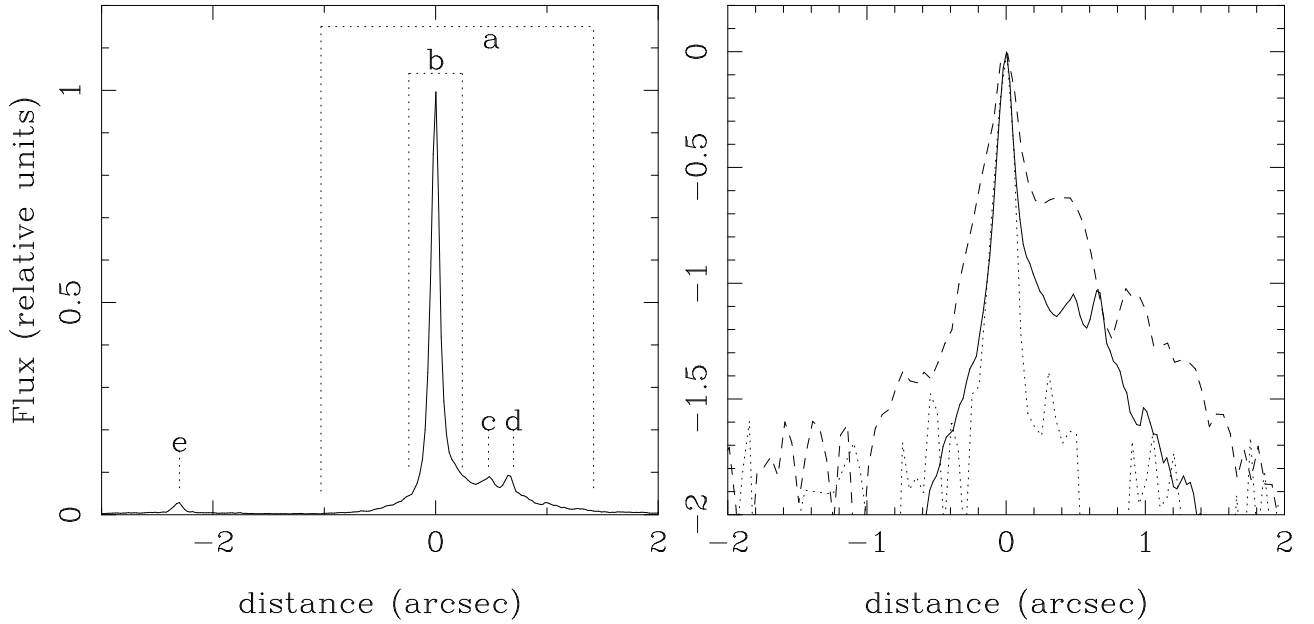


Fig. 4.— a) UV (1500  $\text{\AA}$ ) continuum flux distribution along the slit position. The different extracted one-dimensional spectra are marked in the plot. The flux is normalized to the maximum of the continuum. b) Spatial distribution of the flux (on a logarithmic scale) at the 1500  $\text{\AA}$  UV continuum (full line),  $H\alpha$  flux (dashed line) and the optical continuum near  $H\alpha$  (dotted line). These fluxes have been normalized to their maximum value at the nucleus of the galaxy.

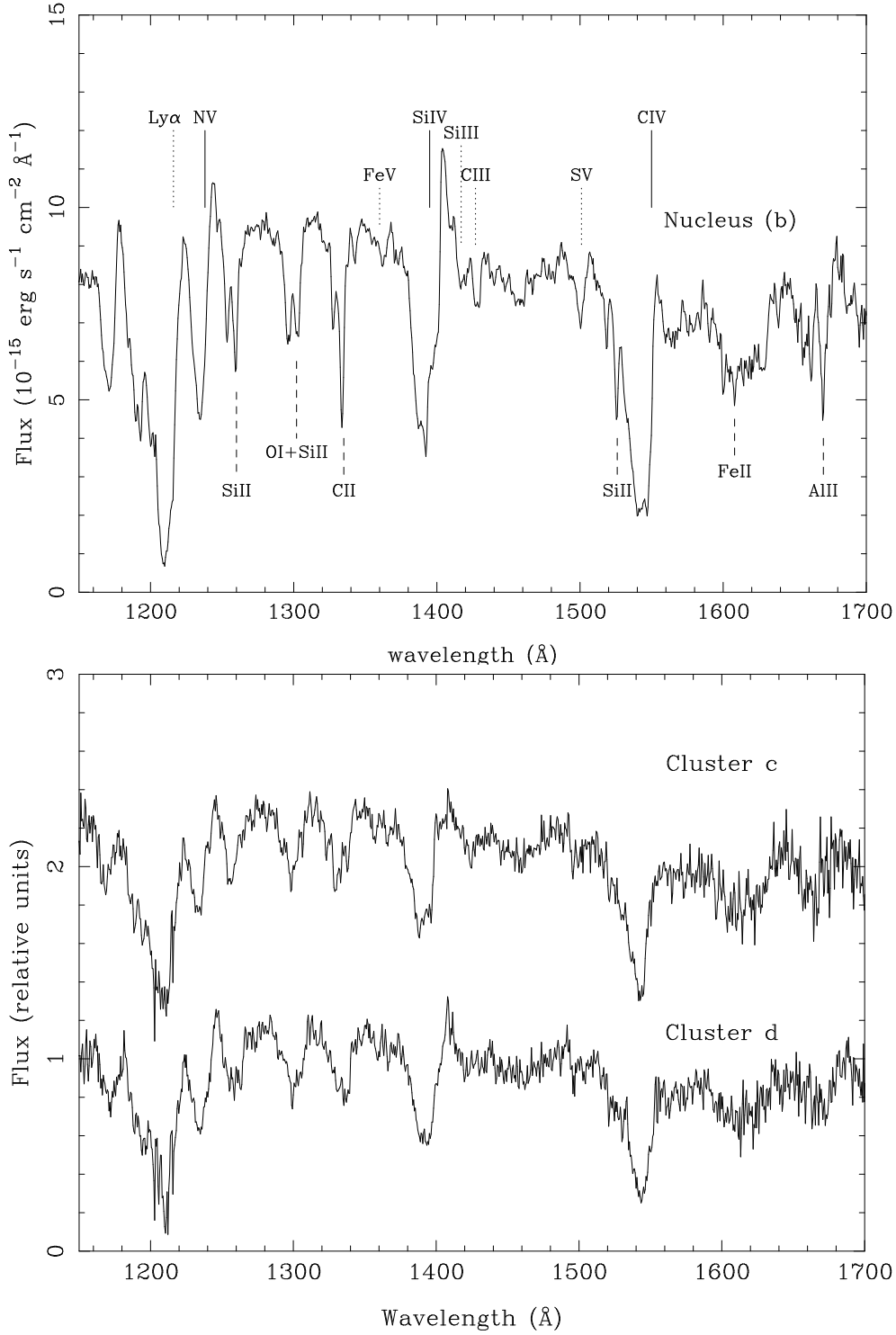


Fig. 5.— a) UV spectrum of the nucleus (marked as b in Figure 4), corresponding to the central  $\pm 0.24$  arcsec. The most important wind (full lines), photospheric (dotted lines) and interstellar lines (dashed lines) are marked in the plot. b) UV spectrum of the clusters marked as c and d in the Figure 4. The flux is in  $1 \times 10^{-15} \text{ erg s}^{-1} \text{ cm}^{-2} \text{ \AA}^{-1}$  units. Cluster c is shifted by  $1 \times 10^{-15} \text{ erg s}^{-1} \text{ cm}^{-2} \text{ \AA}^{-1}$  in the plot.



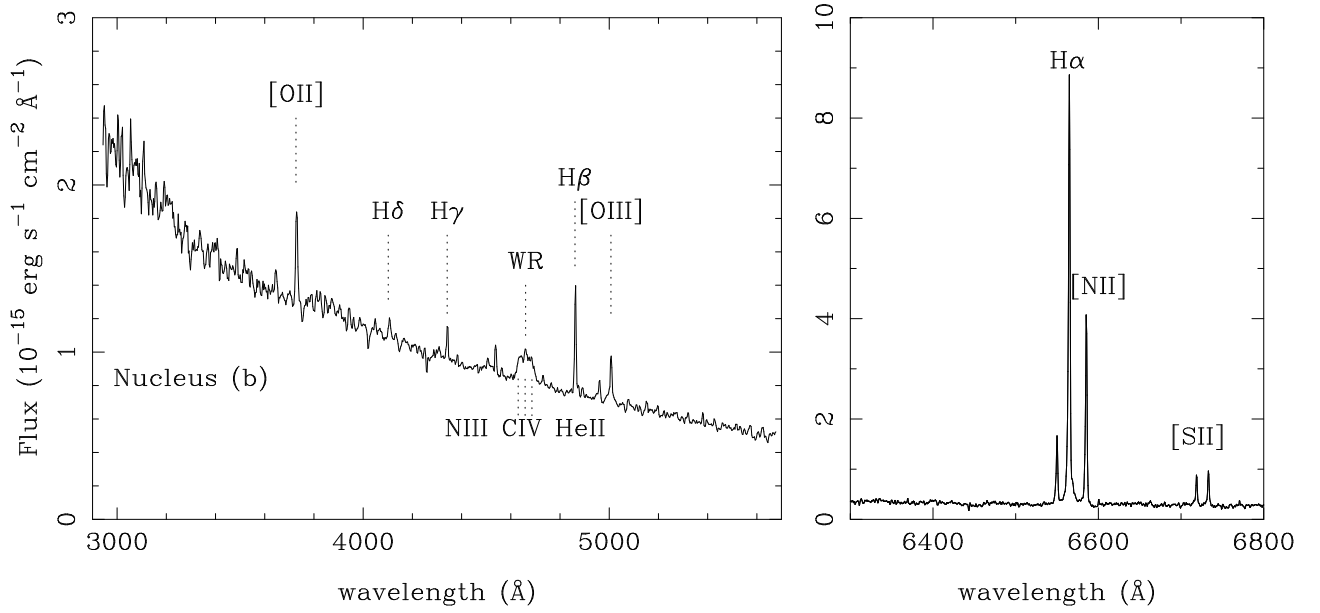


Fig. 6.— Optical continuum of the nucleus (marked as b in Figure 4) at the blue (left) and red (right) wavelength spectral range. The most prominent emission lines and WR features are marked in the plot.

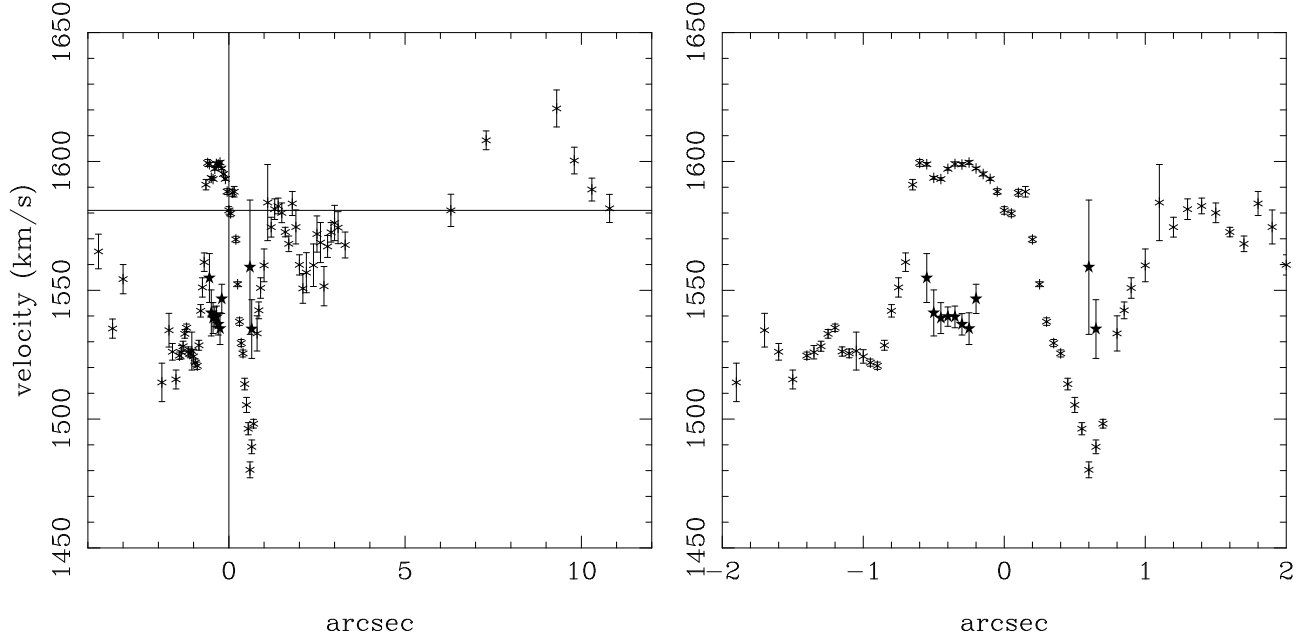


Fig. 7.— Velocity curve of the ionized gas obtained fitting Gaussians to the  $H\alpha$  emission detected along P.A. =  $-138^\circ$ . The second kinematic component of  $H\alpha$  is plotted as stars. The velocity of the continuum peak (the nucleus) is marked by lines. An expansion of the plot corresponding to  $\pm 2$  arcsec is shown on the right.

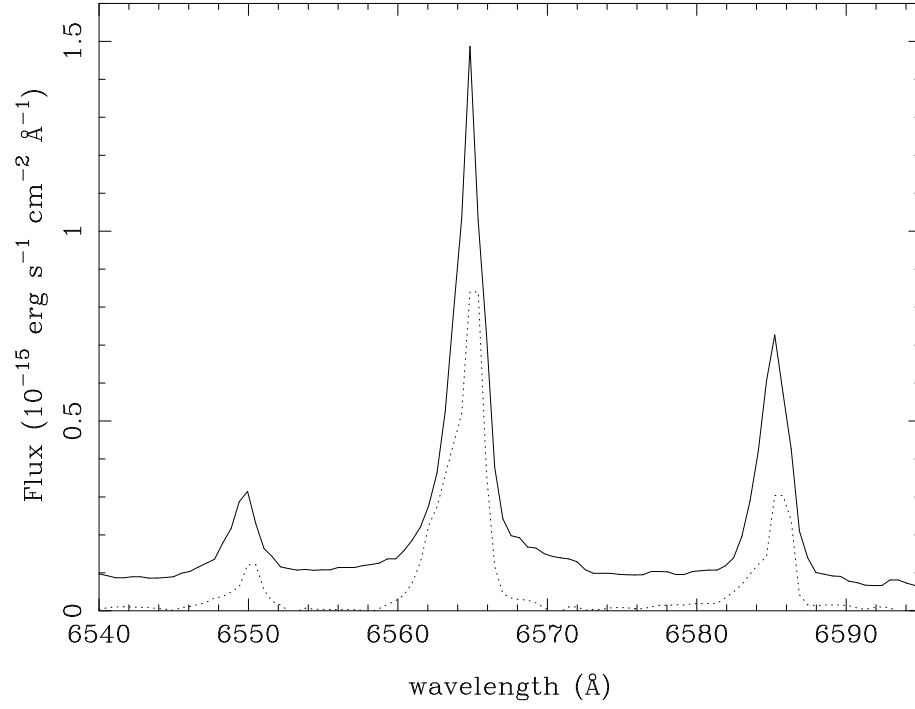


Fig. 8.— Comparison of the profile of  $\text{H}\alpha + [\text{NII}]\lambda 6584, 6548$  at the pixel corresponding to the maximum of the continuum, i.e., the nucleus (full line) with the profile of these lines at 0.35 arcsec south-west of the peak of the continuum (dotted line). The spectrum is plotted in relative units.

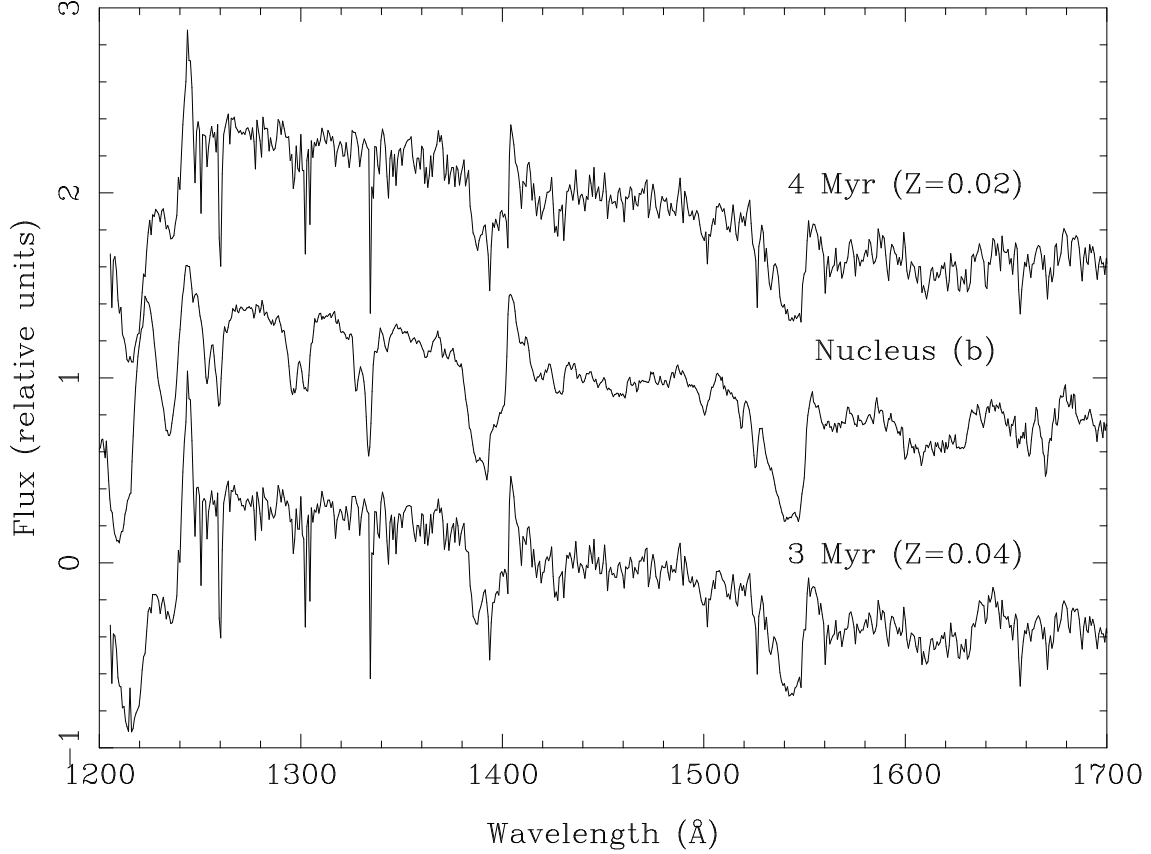


Fig. 9.— STIS/MAMA spectrum of the nucleus (b), corresponding to the UV emission of the central  $0.5 \times 0.5$  arcsec of NGC 3049, de-reddened by  $E(B - V) = 0.2$  using the Calzetti et al. (2000) extinction law and normalized to the corrected flux at  $1500 \text{ \AA}$ . The synthetic 3 Myr and 4 Myr (in relative units) instantaneous burst models fitting the wind lines are also plotted. The models assume that the stars follow a Salpeter IMF with  $M_{\text{up}} = 100 M_{\odot}$  and evolve from the main sequence along the solar ( $Z = 0.02$ ) or the twice solar ( $Z = 0.04$ ) stellar tracks.

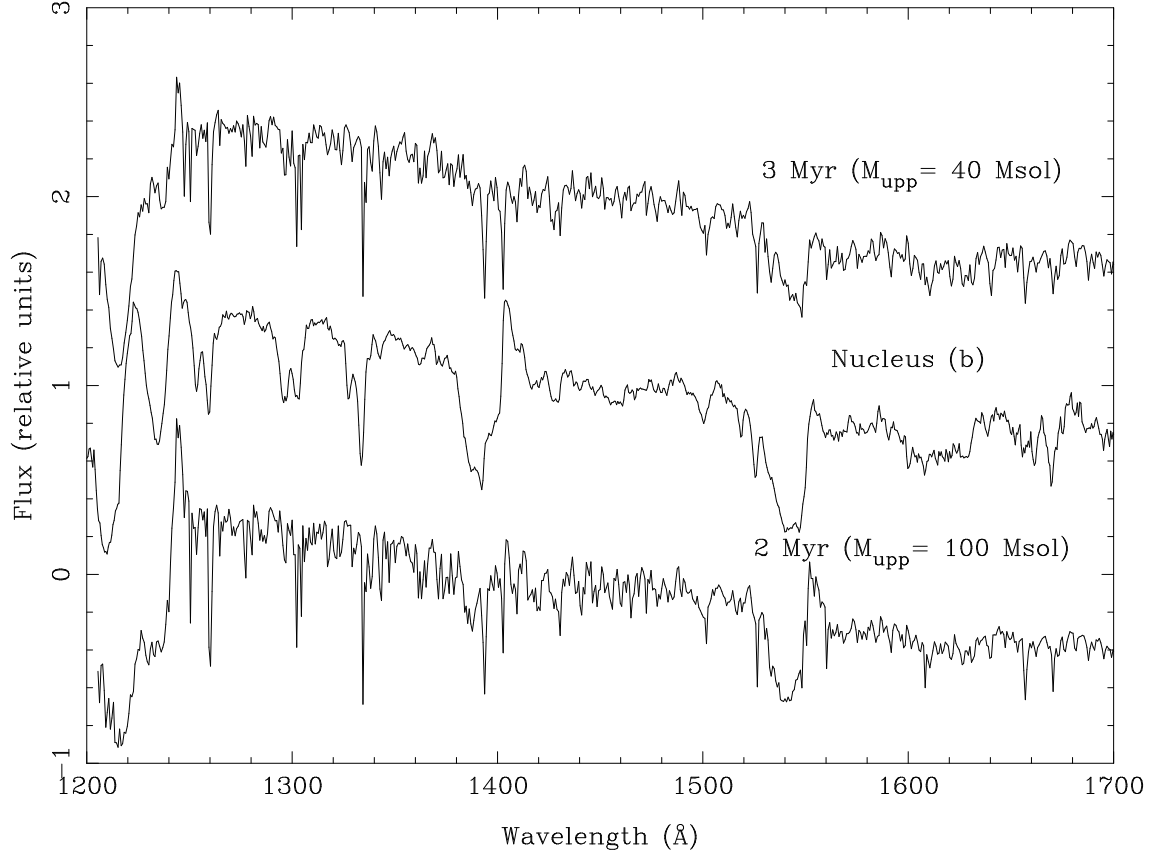


Fig. 10.— The dereddened UV nuclear spectrum is compared with synthetic models ( $Z = 0.02$ ). The IMF is Salpeter with  $M_{\text{up}} = 100 M_{\odot}$  or  $40 M_{\odot}$ . This comparison shows that clusters younger than  $\sim 3$  Myr or having a truncated upper IMF are not compatible with the observed UV wind lines.

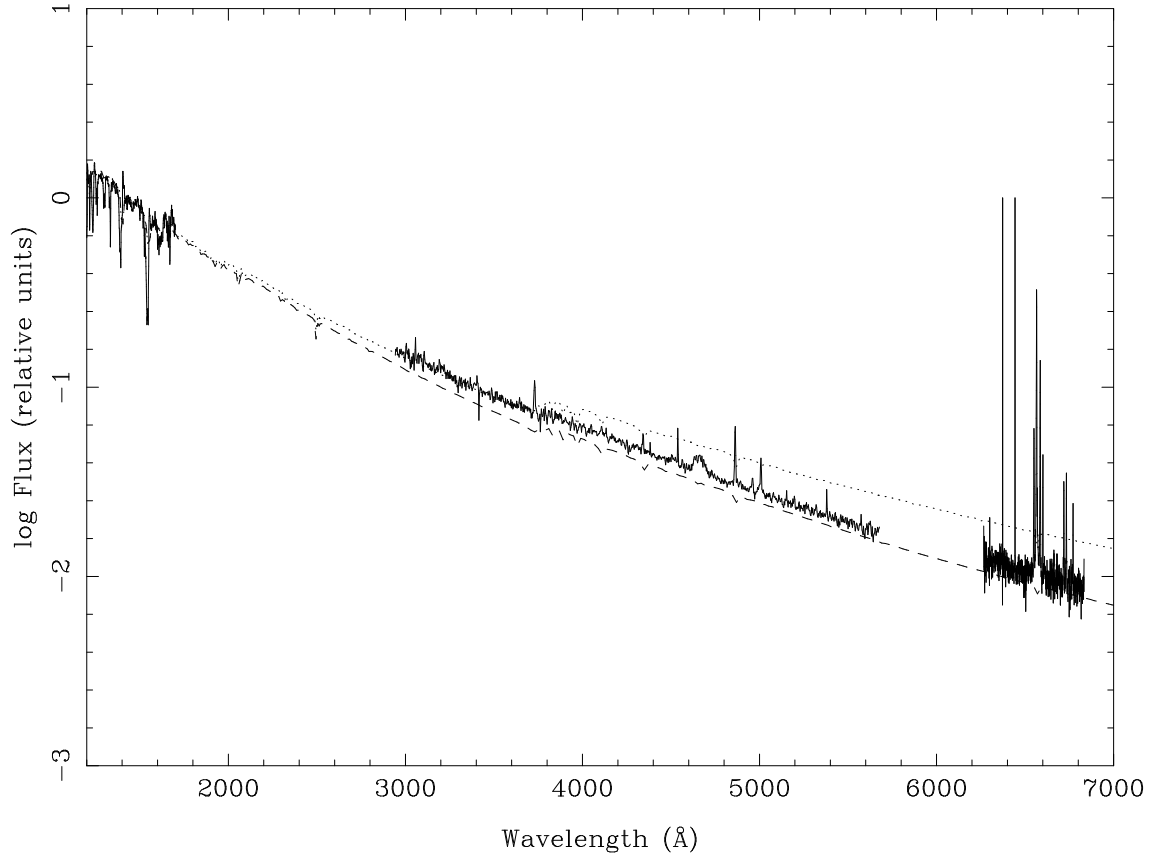


Fig. 11.— Comparison of the UV-optical continuum spectrum  $b$  normalized to the flux at  $1500 \text{ \AA}$  (full line) with the SED of a 3 Myr (dashed line) and 4 Myr (dotted line) old instantaneous burst model having Salpeter IMF,  $M_{\text{up}} = 100 M_{\odot}$ , and  $Z = 0.02$ .

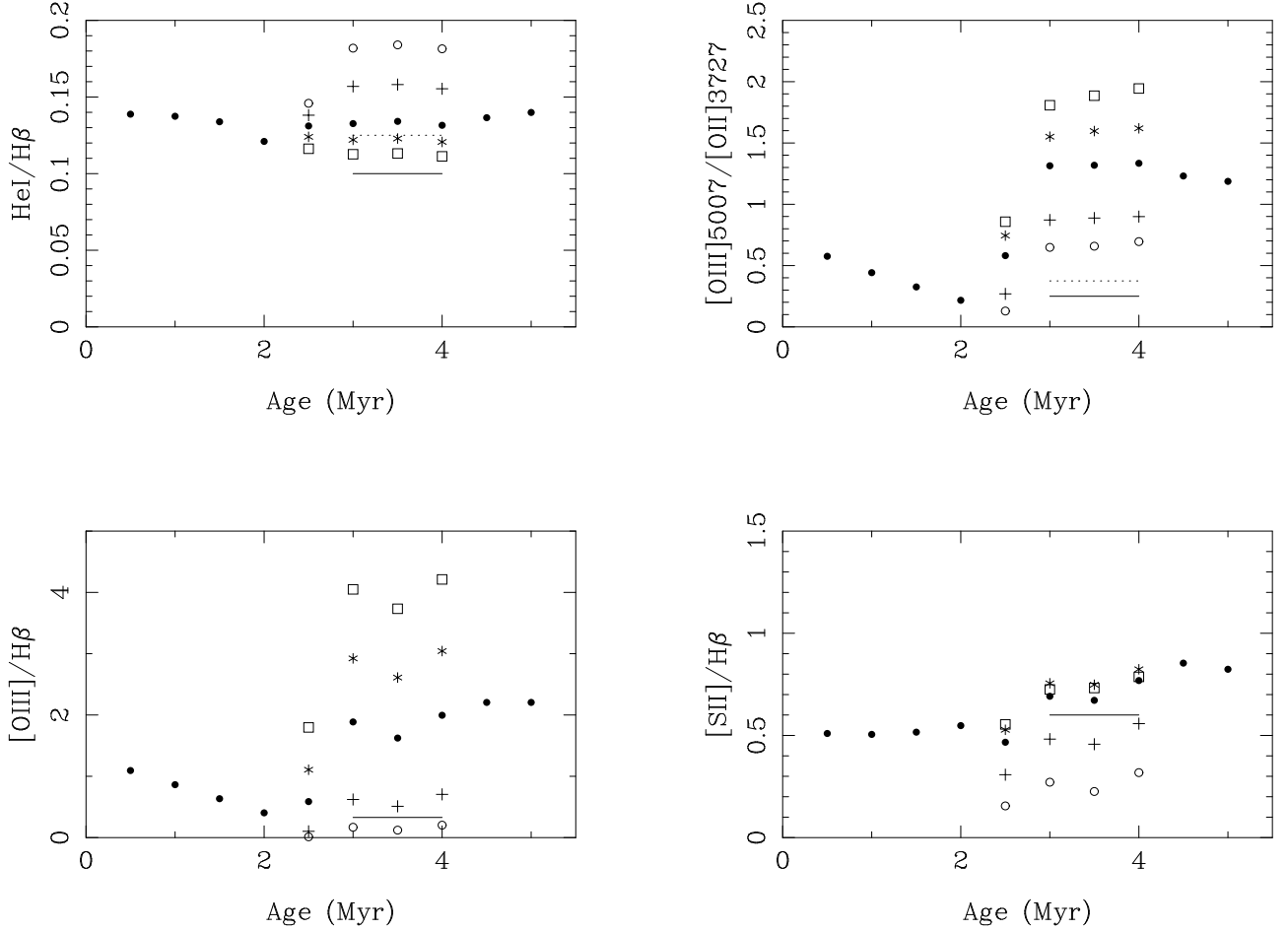


Fig. 12.— Emission-line ratios predicted as a function of age. The observed values are indicated by a horizontal line. Dotted line is the observed value plus the uncertainty associated to the observed emission line ratio. The ionizing cluster formed in an instantaneous burst following a Salpeter IMF with  $M_{\text{up}} = 100 M_{\odot}$ . We assume that the stars have solar metallicity. The oxygen abundance of the gas is  $0.5 Z_{\odot}$  (squares),  $0.75 Z_{\odot}$  (stars),  $Z_{\odot}$  (points),  $1.5 Z_{\odot}$  (crosses) and  $2 Z_{\odot}$  (circles). The abundances of the other elements scale with McGaugh’s (1991) prescription. The filling factor is  $\log \Phi = -2.5$ .

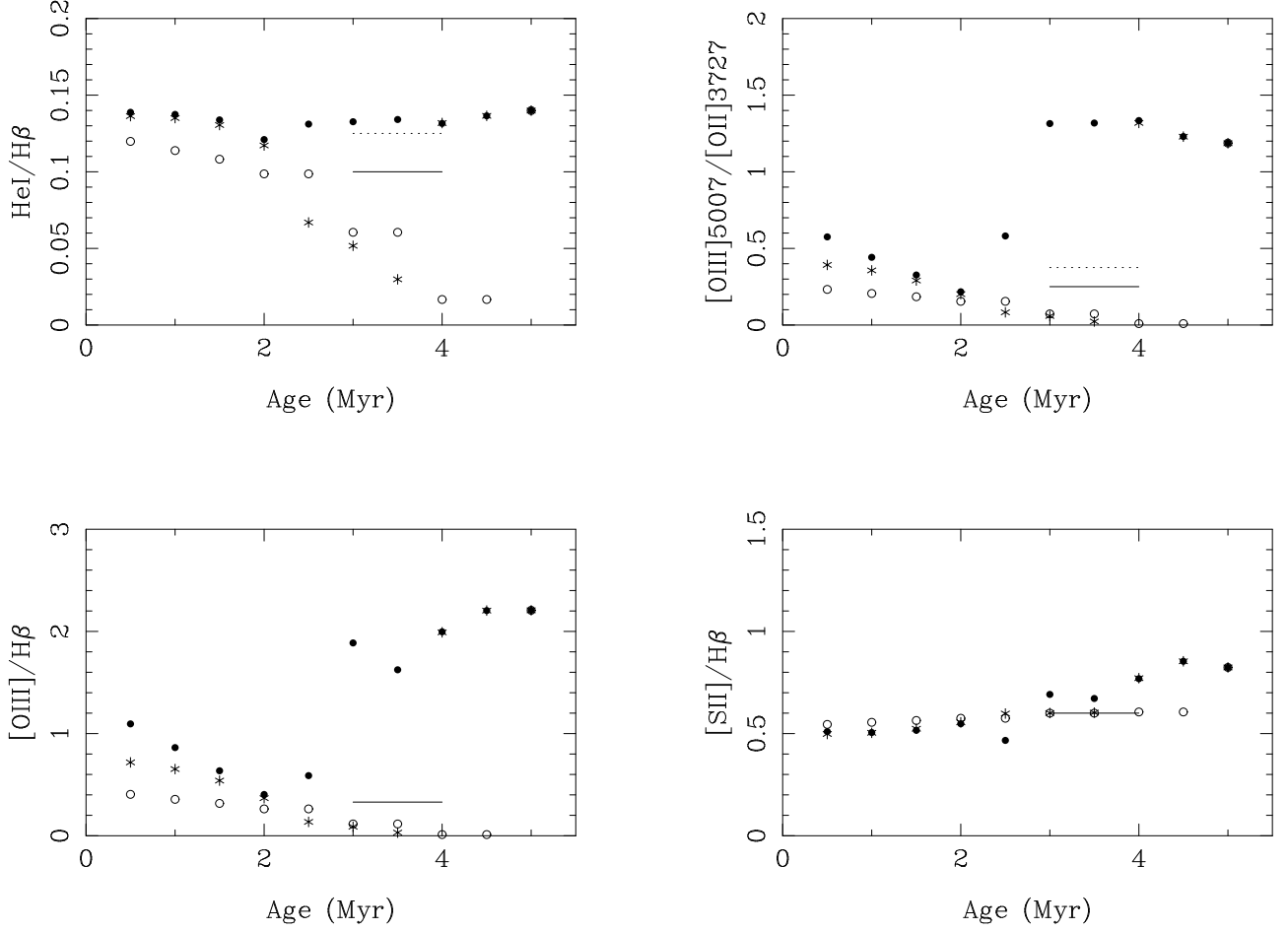


Fig. 13.— Same as Figure 12, but for clusters formed in an instantaneous burst following a Salpeter IMF with  $M_{\text{up}} = 100 M_{\odot}$  (points),  $60 M_{\odot}$  (stars), or  $40 M_{\odot}$  (circles). The oxygen abundance of the gas is  $Z_{\odot}$ .



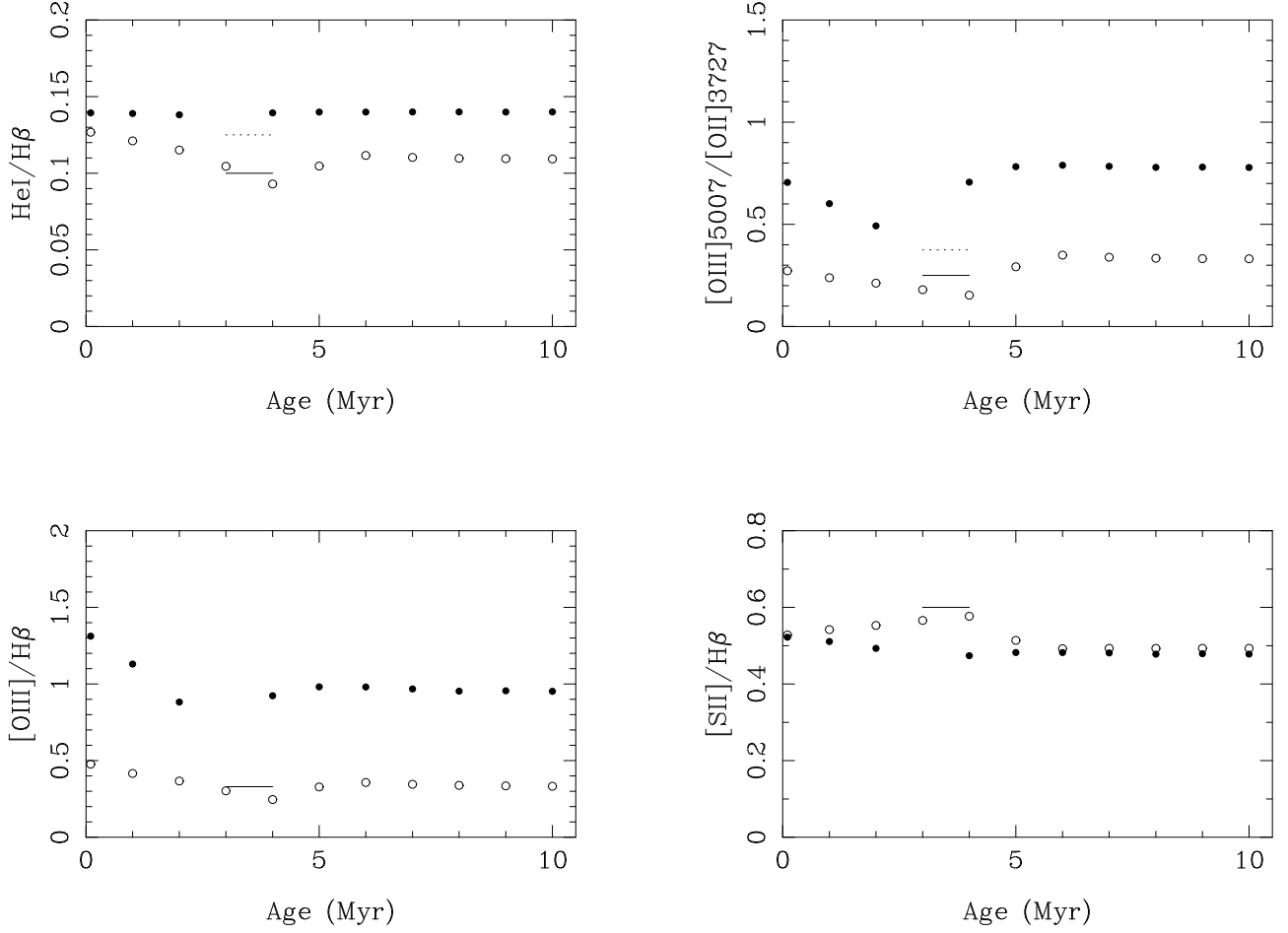


Fig. 14.— Predicted emission-line ratios for continuous star formation and Salpeter IMF with  $M_{\text{up}} = 100 M_{\odot}$  (points) or  $40 M_{\odot}$  (circles). The metallicity is solar.

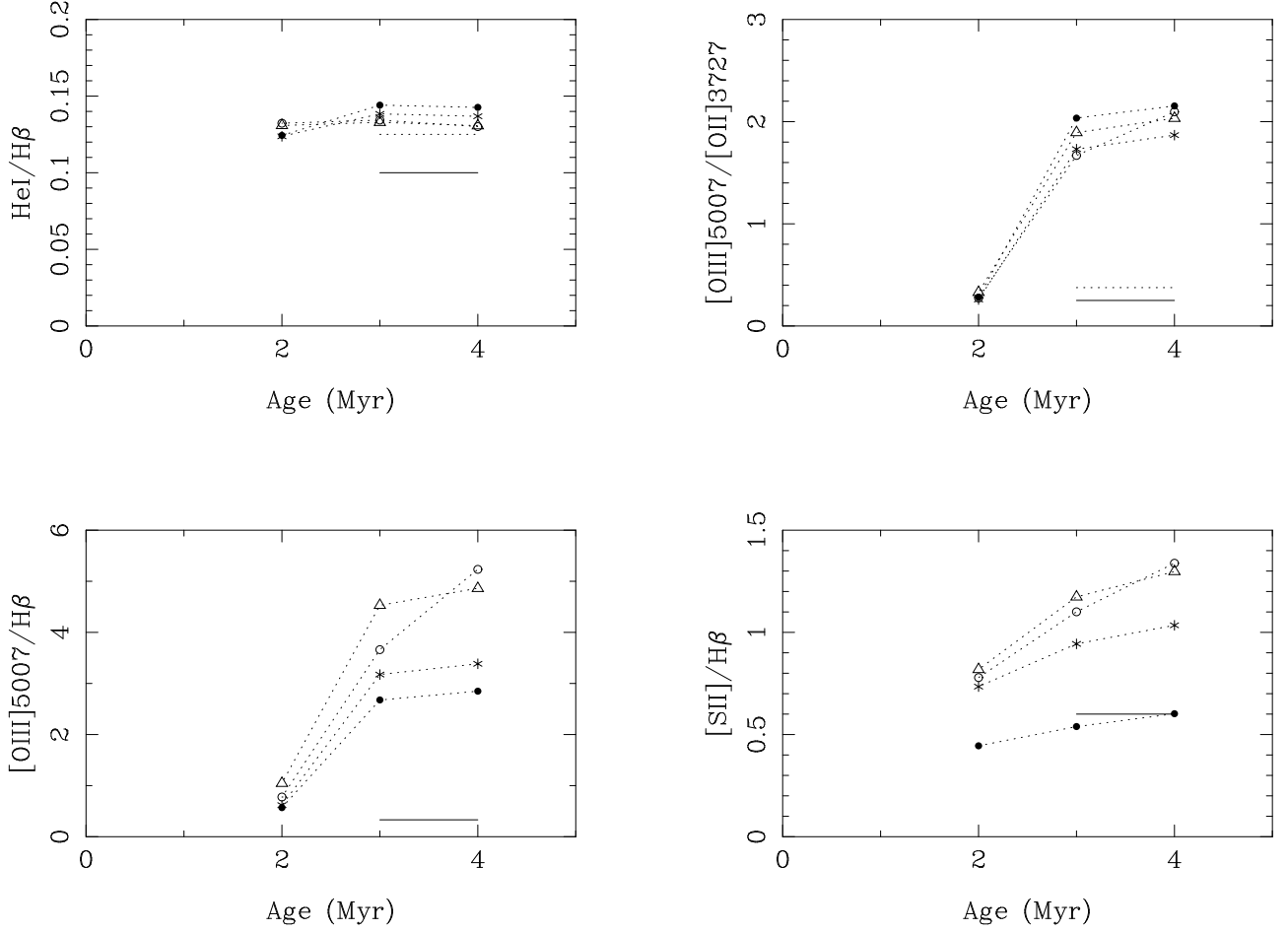


Fig. 15.— Emission-line ratios predicted assuming an instantaneous burst, Salpeter IMF, and  $M_{\text{up}} = 100 M_{\odot}$ . The oxygen abundance of the gas is solar and the other elements scale with the solar ratios. Several dust effects are taken into account in the models. Dust-free models are plotted by points. Models with depletion of the gas-phase abundances are plotted with stars, depletion and grain opacity with circles, and depletion with grain opacity and heating + cooling with triangles.

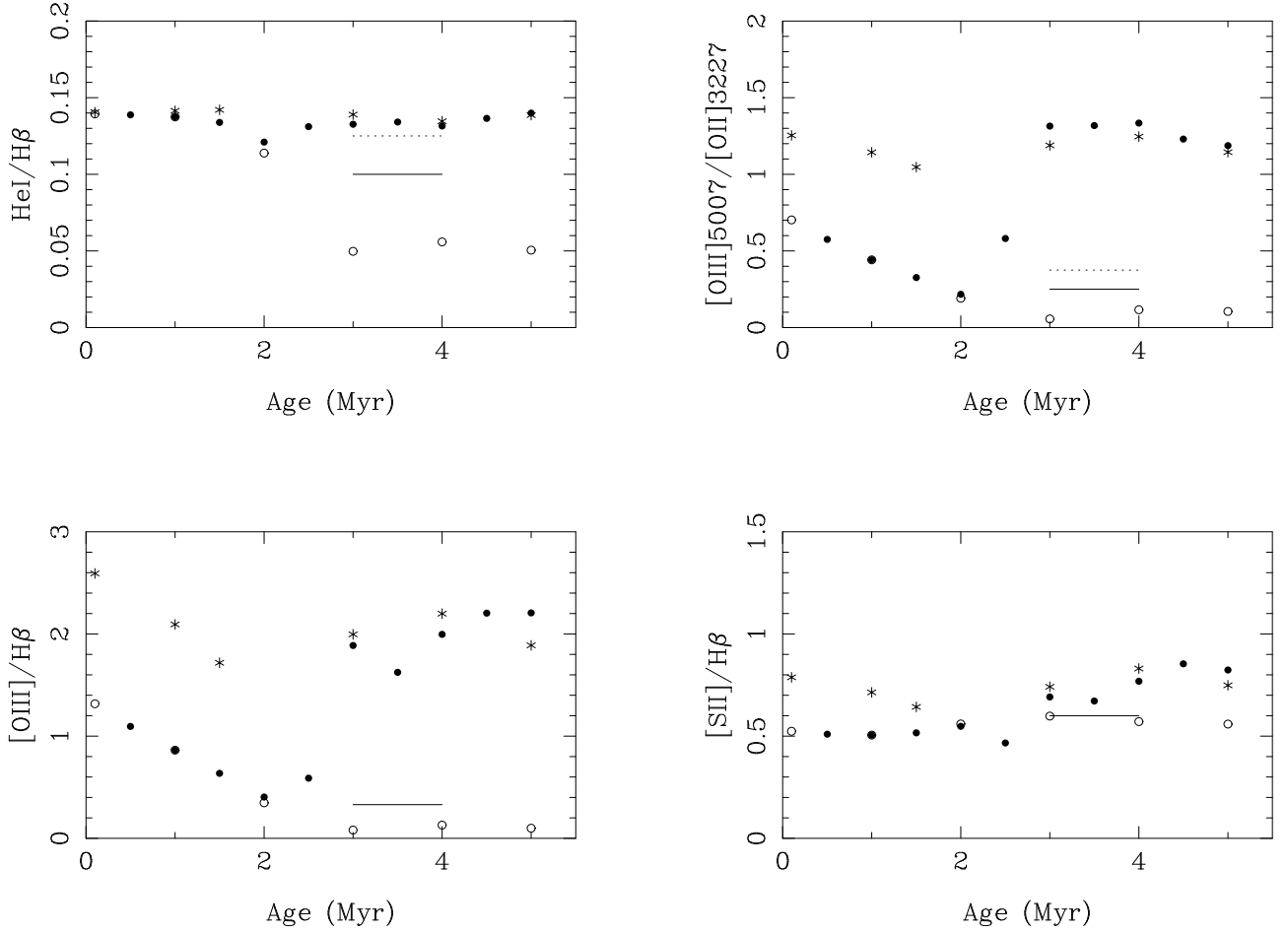


Fig. 16.— Comparison of the emission-line ratios obtained using ionizing radiation fields with different stellar atmosphere models. Predictions using the SED of SB99 with the Lejeune and Schmutz stellar atmospheres are plotted with points, the SED of SB99 with Kurucz atmospheres with circles, and the SED of Schaerer & Vacca (1998) with stars.

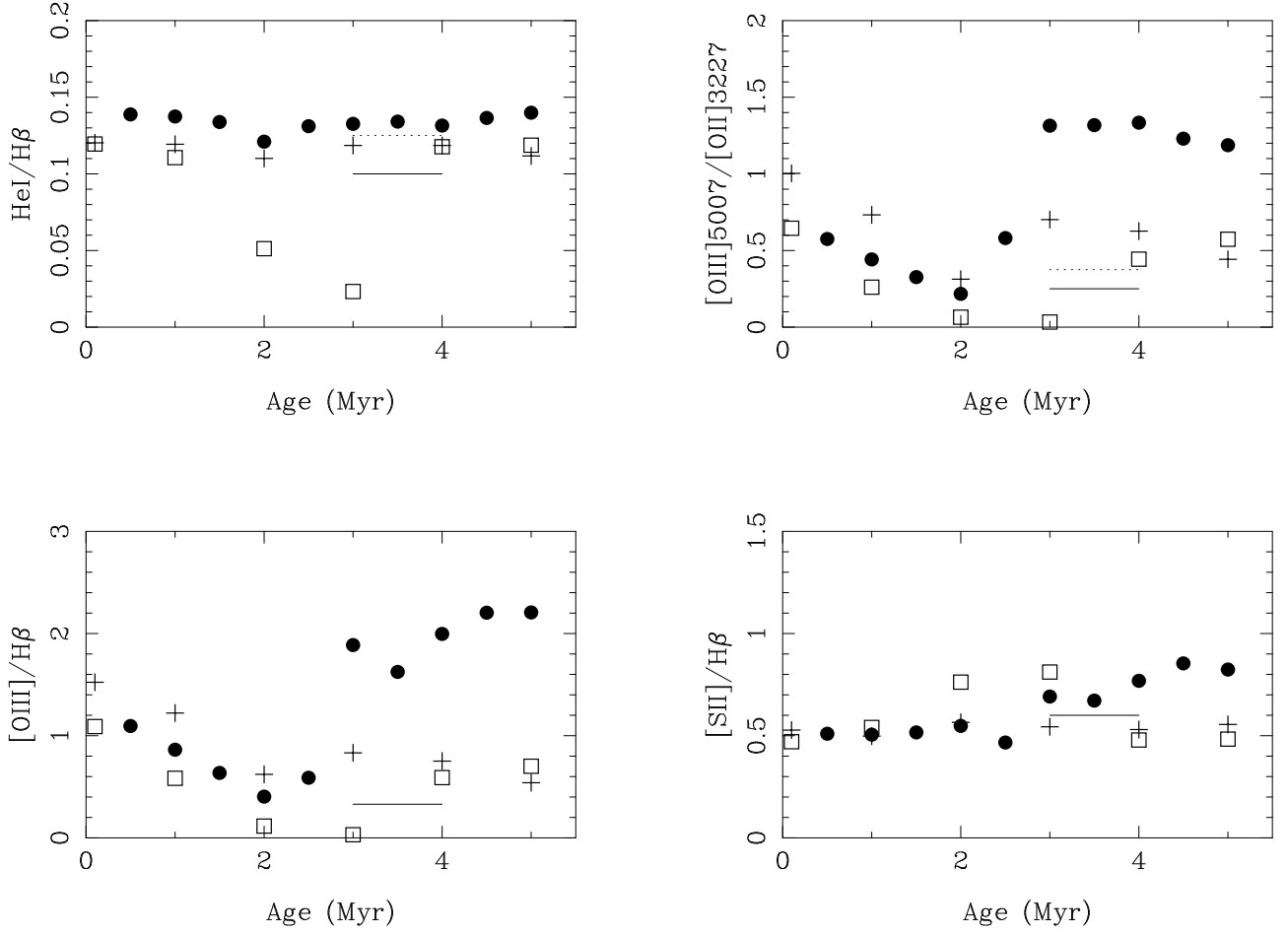


Fig. 17.— Comparison of the emission-line ratios obtained using ionizing radiation fields with different stellar atmosphere models. Predictions using the SED of SB99 with the Lejeune and Schmutz stellar atmospheres are plotted with points, the SED of SB99 with Smith et al (2002) assuming that the stars have solar (twice solar) metallicity are plotted with crosses (squares).

This figure "f1-astroph.gif" is available in "gif" format from:

<http://arxiv.org/ps/astro-ph/0209067v1>

This figure "f2-astroph.gif" is available in "gif" format from:

<http://arxiv.org/ps/astro-ph/0209067v1>

This figure "f3-astroph.gif" is available in "gif" format from:

<http://arxiv.org/ps/astro-ph/0209067v1>